

Electronic Thesis and Dissertation Repository

12-4-2015 12:00 AM

Spectrally-Accurate Algorithm for Flows in 3-Dimensional Rough Channels

Md Nazmus Sakib, *The University of Western Ontario*

Supervisor: J M Floryan, *The University of Western Ontario*

A thesis submitted in partial fulfillment of the requirements for the Master of Engineering Science degree in Mechanical and Materials Engineering

© Md Nazmus Sakib 2015

Follow this and additional works at: <https://ir.lib.uwo.ca/etd>



Part of the [Mechanical Engineering Commons](#)

Recommended Citation

Sakib, Md Nazmus, "Spectrally-Accurate Algorithm for Flows in 3-Dimensional Rough Channels" (2015). *Electronic Thesis and Dissertation Repository*. 3366.
<https://ir.lib.uwo.ca/etd/3366>

This Dissertation/Thesis is brought to you for free and open access by Scholarship@Western. It has been accepted for inclusion in Electronic Thesis and Dissertation Repository by an authorized administrator of Scholarship@Western. For more information, please contact wlsadmin@uwo.ca.

Spectrally-Accurate Algorithm for Flows in 3-Dimensional Rough Channels

(Thesis format: Monograph)

by

Md Nazmus Sakib

Graduate Program in Mechanical and Materials Engineering

A thesis submitted in partial fulfillment
of the requirements for the degree of
Masters of Engineering Science

The School of Graduate and Postdoctoral Studies
The University of Western Ontario
London, Ontario, Canada

© Md Nazmus Sakib 2016

Abstract

In this work a spectrally accurate algorithm has been developed for the simulation of three-dimensional flows bounded by rough walls. The algorithm is based on the velocity-vorticity formulation and uses the concept of Immersed Boundary Conditions (IBC) for the enforcement of the boundary conditions. The flow domain is immersed inside a fixed computational domain. The geometry of the boundaries is expressed in terms of double Fourier expansions and boundary conditions enter the algorithm in the form of constraints. The spatial discretization uses Fourier expansions in the stream-wise and span-wise directions and Chebyshev expansions in the wall-normal direction. The algorithm can use either the fixed flow rate constraint or the fixed pressure gradient constraint; a direct implementation of the former constraint is described. An efficient solver which takes advantage of the structure of the coefficient matrix has been developed. Taking the advantage of the reality conditions enhances the efficiency of the solver both in terms of memory and computational speed. It is demonstrated that the applicability of the algorithm can be extended to more extreme geometries using the over-determined formulation. Various tests confirm the spectral accuracy of the algorithm.

Keywords

Spectral method, immersed boundary conditions method, rough boundaries, three-dimensional channels. Efficient solver, using reality conditions, over-determined formulation.

Co-Authorship Statement

This dissertation is prepared in monograph format and is based on a manuscript that has been submitted for publication.

N. Sakib, A. Mohammadi and J. M. Floryan, “Spectrally Accurate Immersed Boundary Conditions Method for Three-Dimensional Flows”, submitted for publication in the Journal of Computational Physics. Manuscript Number: JCOMP-D-15-01411.

Dedication

To my parents and siblings for the love, support and encouragement.

Acknowledgments

I am grateful to my supervisor Prof. J. M. Floryan for his assistance and encouragement. This work would not have been possible without his continual support and guidance.

I would like to express my gratitude to the members of my advisory committee, Prof. A. G. Straatman and Prof. E. Savory for their invaluable suggestions and insightful comments.

I would also like to thank my colleagues Alireza Mohammadi, Hadi Vafadar Moradi, Mohammad Zakir Hossain, Sahab Zandi, Amirreza Seddighi and Seyed Arman Abtahi for their friendship, support and motivation. I am particularly indebted to Alireza Mohammadi for his guidance throughout this whole work.

Finally, I would like to mention that this work has been carried out with support from the Natural Sciences and Engineering Research Council (NSERC).

Table of Contents

Abstract	ii
Co-Authorship Statement	iii
Dedication	iv
Acknowledgments	v
Table of Contents	vi
List of Figures	viii
List of Appendices	xi
List of Abbreviations, Symbols and nomenclature	xii
Section 1	1
1 Introduction	1
Section 2	5
2 Problem Formulation	5
2.1 Geometry of the Flow Domain	5
2.2 Governing Equations	6
2.3 Flow in a Smooth Channel	7
2.4 Flow between Rough Walls	7
Section 3	10
3 Numerical Solution of the Problem	10
3.1 Forms of the Governing Equations Suitable for the Numerical Solution	10
3.2 Discretization Method	12
3.2.1 Discretization of the Field Equations	14
3.2.2 Discretization of the Boundary Conditions	21
3.2.3 Discretization of the Flow Rate Constraint	24
Section 4	31

4 Solution Process	31
4.1 Specialized Direct Solver	32
4.2 Implementation of the Reality Conditions	36
Section 5	39
5 Evaluation of the Pressure Field	39
Section 6	41
6 Performance of the Algorithm	41
Section 7	53
7 Over-determined Formulation	53
Section 8	59
8 Limitations of the Algorithm	59
Section 9	60
9 Conclusion	60
References	62
Appendices	66
Appendix A	66
Appendix B	67
Appendix C	67
Curriculum Vitae	70

List of Figures

Figure 1: Sketch of the flow and computational domain.....	6
Figure 2: Structure of the coefficient matrix L for $N_T = 30$, $N_M = M_M = 1$. For the fixed pressure gradient constraint (Fig. 2A) $p = (2N_M + 1)(2M_M + 1)2N_T$ and for the fixed flow rate constraint (Fig. 2B) $p = (2N_M + 1)(2M_M + 1)2N_T + 2$. The black color identifies the non-zero elements with nz giving their total number. The blocks assume various shades of grey depending on the density of the non-zero elements.....	33
Figure 3: The structure of the re-arranged coefficient matrix for $N_T = 30$, $N_M = M_M = 1$. The black color identifies the non-zero elements with nz giving their total number. The blocks assume various shades of grey depending on the density of the non-zero elements...	35
Figure 4: Schematic diagram of the coefficient matrix for the fixed pressure gradient constraint with all unknowns separated into real and imaginary parts. Each small block contains coefficients of the unknowns written in the block.....	37
Figure 5: Variations of the computational time per iteration (Fig. 5A) with and without taking advantage of the complex conjugate property and variations of the memory savings when taking advantage of the complex conjugate property (Fig. 5B) as functions of the number of Fourier modes used in the solution. $N_T = 50$ Chebyshev polynomials have been used in the tests.	38
Figure 6: Geometry of the lower wall described by (6.1) with $y_b = 0.1$, $\alpha = \beta = 1$ for two periods in the x - and z -directions.	41
Figure 7: Difference between the velocity fields obtained by current algorithm and algorithm described by [14] for transverse grooves at narrowest channel opening (Fig.7A) and widest channel opening (Fig.7B). Calculations have been carried out with $y_b = 0.05$ and $\alpha = 1$ for $Re = 5$	42

Figure 8: Difference between the velocity fields obtained by current algorithm and algorithm described by [14, 15, 35] for transverse grooves at narrowest channel opening (Fig.8A) and widest channel opening (Fig.8B). Calculations have been carried out with $y_b = 0.05$ and $\beta = 1$ for $Re = 5$ 42

Figure 9: Variation of $\|u_{er}\|_\infty$ as a function of the number of Chebyshev polynomials N_T used in the solution. Calculations have been carried out with $N_M = M_M = 10$ for the roughness geometry described by (6.1) with $\alpha = \beta = 1$ for $Re = 5$ 44

Figure 10: Variation of the modal functions close to the rough boundary. Calculations have been carried out with $N_T = 40$ for the roughness geometry described by (5.1) $\alpha = \beta = 1$, $y_b = 0.1$ for $Re = 5$. In Fig. 8A, m changes while $n = 10$ and in Fig.8B n changes while $m = 10$. Formation of boundary layers near the rough wall and rapid growth of modal functions across these layers are clearly visible. 45

Figure 11: Variation of the Chebyshev norm of the modal function $v^{(n,m)}$ as a function of the Fourier mode index $n = m$ for the roughness geometry described by (6.1) with $\alpha = \beta = 1$ for $Re = 5$. Computations have been carried out with $N_M = M_M = 12$ Fourier modes and $N_T = 40$ Chebyshev polynomials..... 46

Figure 12: Variation of $\|u_{er}\|_\infty$ and $\|u_{er,BC}\|_\infty$ as a function of the number of Fourier modes used in the computations for the roughness geometry described by (5.1) with $\alpha = \beta = 1$ for $Re = 5$. Calculations have been carried out using $N_T = 40$, and $M_M = 10$ (Fig. 10A) and $N_M = 10$ (Fig. 10B)..... 47

Figure 13: Distributions of the boundary errors $u_{er,BC}(x, z)$ (Fig. 11A), $v_{er,BC}(x, z)$ (Fig. 11B) and $w_{er,BC}(x, z)$ (Fig.11 C) for the roughness geometry described by (5.1) with $\alpha = \beta = 1$ for $Re = 5$ over one period in the x - and z -directions. 49

Figure 14: Spectral decomposition of $u_{er,BC}(x, z)$ for the roughness geometry described by (6.1) with $\alpha = \beta = 3$, $y_b = 0.1$ for $Re = 5$. Results displayed in Fig. 12A have been obtained using computational box with $\alpha = \beta = 3$, $N_M = 8$ and $M_M = 7$ Fourier modes and those displayed in Fig.12B have been obtained using computational box with $\alpha = \beta = 1.5$,

$N_M = 16$ and $M_M = 14$ Fourier modes. In both cases, $N_T = 35$ Chebyshev polynomials were used. 50

Figure 15: Variations of the error norm $\|u_{er,BC}\|_\infty$ as a function of the roughness amplitude y_b (Fig.13 A) and as a function of the roughness wave number with $\alpha = \beta$ (Fig.13 B) for the roughness geometry described by (6.1). Calculations have been carried out using $N_T = 40$ Chebyshev polynomials and $N_M = M_M = 5$ (solid lines) and $N_M = M_M = 10$ (dash lines) Fourier modes. 51

Figure 16: Variation of the error norm $\|u_{er,BC}\|_\infty$ as a function of the Reynolds number Re for the roughness geometry described by (6.1) with $\alpha = \beta = 1$ and different values of y_b . Computations have been carried out using $N_T = 50$ Chebyshev polynomials and $N_M = M_M = 10$ Fourier modes. 52

Figure 17: Structure of the coefficient matrix L_0 for the over-determined formulation with $N_M = M_M = 1$, $NM_o = MM_o = 2$ and $N_T = 30$. Black color represents the non-zero elements with nz denoting their number. Figure 15A displays the initial form of the matrix while Fig. 15B shows the form after extractions of the largest diagonal matrix A from H . The blocks assume various shades of grey depending on the density of the non-zero elements... 56

Figure 18: Spectral decomposition of $u_{er,BC}(x, z)$ at the rough wall for the roughness geometry described by (6.1) with $\alpha = \beta = 5$, $y_b = 0.05$ for $Re = 10$. Computations have been carried out using $N_T = 50$ Chebyshev polynomials, $N_M = M_M = 10$ Fourier modes for the field equations, and $NM_o = MM_o = 15$ Fourier modes for the boundary conditions. 57

Figure 19: Variations of the error norm $\|u_{er,BC}\|_\infty$ as a function of the roughness amplitude y_b (Fig.17 A) for the roughness geometry described by (6.1) with $\alpha = \beta = 4$ for $Re = 10$ and as a function of the roughness wave number $\alpha = \beta$ (Fig.17 B) for the roughness amplitude $y_b = 0.08$. Calculations have been carried out using $N_T = 50$ Chebyshev polynomials and $N_M = M_M = 12$ Fourier modes for the field equations. 58

List of Appendices

Appendix A: Analysis of Mode (0,0).....	64
Appendix B: Determination of Chebyshev Expansion Coefficient for a Known Modal Function	65
Appendix C: Evaluation of Fourier expansions representing periodic functions formed by the values of the Chebyshev polynomials, its derivatives and the reference flow velocity evaluated along the rough boundary	65

List of Abbreviations, Symbols and nomenclature

Abbreviations

IB	Immersed boundary
IBC	Immersed boundary conditions
RF	Relaxation factor
FFT	Singular value decomposition
SVD	Singular value decomposition

Nomenclatures used in Section 2

(x, y, z)	Physical coordinate system
y_U, y_L	Shape of the upper wall in the physical coordinate system
α, β	Wave numbers in the x - and z -directions
λ_x, λ_z	Wave lengths in x - and z -directions
N_A, M_A	Number of Fourier modes used in the x - and z -direction to describe the roughness geometry
$H_U^{(n,m)}, H_L^{(n,m)}$	Fourier expansion coefficients of the upper and lower wall in the physical coordinate system.
L	Mean channel opening
U_{max}	Maximum velocity of the reference flow in the direction of total pressure gradient
Re	Reynolds number
ρ, ν	Density and kinematic viscosity

\vec{V}_0, \vec{V}	Reference velocity vector and total velocity vector
u, v, w	Components of total velocity in the x -, y - and z -directions
u_0, v_0, w_0	Components of reference velocity in the x -, y - and z -directions
u_1, v_1, w_1	Modification velocity components in the x -, y - and z -directions
p, p_0, p_1	Total pressure, reference pressure and pressure modification
e_x, e_z	Mean pressure gradient components in the x - and z -directions
e'_x, e'_z	Modifications of the mean pressure gradient components in the x - and z -directions
$Q(x) _{mean}$	Mean flow rate in the x - and z -directions
Q_{x0}, Q_{x1}	Reference flow rate and flow rate modification in the x -direction
Q_{z0}, Q_{z1}	Reference flow rate and flow rate modification in the z -direction
$\partial_x p _{mean}$	Mean Pressure gradient in the x -direction

Nomenclatures used in Section 3

$\vec{\omega}, \vec{\omega}_0, \vec{\omega}_1$	Vorticity vector for total flow, reference flow and flow modification
$\omega_x, \omega_y, \omega_z$	Components of total vorticity in the x -, y - and z -directions
$\xi_1, \eta_1, \varsigma_1$	Components of modification vorticity in the x -, y - and z -directions
N_η, N_v	Nonlinear terms associated with vorticity and velocity equation

H_u, H_v, H_w	Nonlinear terms associated with x -, y - and z -momentum equations
(x, \hat{y}, z)	Computational coordinate system
Γ	Constant for coordinate transformation
y_t, y_b	Locations of extremities for the upper and lower wall
\hat{y}_U, \hat{y}_L	Shape of the upper and lower wall in the transformed coordinate system
$A_U^{(n,m)}, A_L^{(n,m)}$	Fourier expansion coefficients of the upper and lower wall in the transformed coordinate system.
$\eta^{(n,m)}, u^{(n,m)}, v^{(n,m)}, w^{(n,m)}$	Modal functions for wall-normal vorticity, and the modification velocity components in the x -, y - and z -directions
D	Derivative with respect to the transverse direction
$\langle u_1 u_1 \rangle^{(n,m)}, \langle u_1 v_1 \rangle^{(n,m)}$	
$\langle u_1 w_1 \rangle^{(n,m)}, \langle v_1 v_1 \rangle^{(n,m)}$	Modal functions of the velocity products
$\langle v_1 w_1 \rangle^{(n,m)}, \langle w_1 w_1 \rangle^{(n,m)}$	
$\eta_k^{(n,m)}, u_k^{(n,m)}, v_k^{(n,m)}, w_k^{(n,m)}$	Chebyshev expansion coefficients of the modal functions representing the vorticity and velocity components
T_k	k^{th} Chebyshev polynomial of first kind
N_T	Order of Chebyshev polynomials used for discretization of the modal function in the \hat{y} -direction

$(G_{uu})_k^{(n,m)}, (G_{uv})_k^{(n,m)},$ $(G_{uw})_k^{(n,m)}, (G_{vv})_k^{(n,m)},$ $(G_{vw})_k^{(n,m)}, (G_{ww})_k^{(n,m)}$	Chebyshev expansion coefficients of the modal functions of the velocity products
ω	Weight function
$(U_0^U), (W_0^U)$	Coefficient of Fourier expansions for $u_0(\hat{y}_U(x, z))$ and $w_0(\hat{y}_U(x, z))$
$(CU)_k^{(n,m)}, (CL)_k^{(n,m)}$	Coefficients of Fourier expansions for the Chebyshev polynomials at the upper and lower wall.
$(EU)_k^{(n,m)}, (EL)_k^{(n,m)}$	Coefficients of Fourier expansions for the first derivative of the Chebyshev polynomials at the upper and lower wall.
$Q_x(x)$	Flow rate in the x -direction
$Q_x^{(n)}$	Fourier expansion coefficient of the flow rate in the x -direction

Nomenclatures used in Section 4

L, X, R	Coefficient matrix vector of unknowns and right-hand side vector
A, B, C, D	Sections of rearranged coefficient matrix
X_1, X_2	Vector of unknowns for the rearranged system of equations
R_1, R_2	Right-hand side vectors for the rearranged system of equations
$\eta_r^{(n,m)}, u_r^{(n,m)}, v_r^{(n,m)}$	Real part of the modal functions for wall-normal vorticity and

$w_r^{(n,m)}$	the three velocity components.
$\eta_i^{(n,m)}, u_i^{(n,m)}, v_i^{(n,m)}$	Imaginary part of the modal functions for wall-normal vorticity and the three velocity components.
$w_i^{(n,m)}$	

Nomenclatures used in Section 6

$\ u_{er}\ _\infty$	Error norm for the whole physical domain
$\ u_{er,BC}\ _\infty$	Error norm for the boundary
$u_{er}(x, y, z)$	Error for whole physical domain
$u_{er,BC}(x, z)$	Error at the rough boundary
$u_{computed}(x, y, x)$	Computed solution for the whole physical domain
$u_{reference}(x, y, z)$	Reference solution for the whole physical domain
$u_{computed}(x, y_L(x, z), z)$	Solution computed at the rough boundary

Nomenclatures used in Section 7

NM_o, MM_o	Number of Fourier modes used for boundary constraints in the x - and z -directions for the over-determined formulation
L_0, X, R_0	Coefficient matrix, vector of unknowns and right-hand side vector for the over-determined system
H, K_0	Sections of rearranged coefficient for the over-determined system

L_0^+	Generalized inverse of L_0
Q, R, R_1	Matrices used in QR factorization
U, S, V, S_1	Matrices used in SVD method
A, B, C_0, D_0	Sections of the rearranged coefficient matrix L_0
H	Conjugate transpose as superscript

Section 1

1 Introduction

Roughness can be found in almost every type of flow systems. They have the ability to enhance or deteriorate the functionality of a flow system. The history of the study of the effect of surface roughness on fluid flow dates back to the works of Hagen and Darcy [1, 2] who concluded that roughness always increases flow resistance. The quantification of average drag in terms of friction factor was accomplished by Nikuradse and Moody [3, 4] who also demonstrated that the drag in laminar flow regime is independent of surface roughness.

The prevailing belief of surface roughness always increasing drag was first contradicted by Walsh [5, 6]. His experiments on flows over stream-wise grooves in the form of riblets demonstrated that surface roughness can reduce turbulent drag. In their works on drag reducing longitudinal grooves (riblets), Choi, Moin and Kim [7] and Chu and Karniadakis [8] concluded that though these kinds of grooves have the capability to reduce turbulent drag, they always increase laminar drag.

The pressure losses for laminar flows over rough surfaces regained the focus because of the growing interest on the flows in micro-channels and the deviation from the classical theory found in the works of Papautsky et al, Sobhan and Garimella, Morini, Sharp and Adrian, and Gamrat et al [9-13]. Mohammadi and Floryan [14] investigated the pressure losses in grooved channels for laminar flows and found the potential to obtain laminar drag reducing grooves by proper shaping of the grooves. Mohammadi and Floryan [15] also studied the drag reducing longitudinal grooves and determined the optimal shape for such kind of grooves.

The main difficulty associated with the numerical solution of flow problems bounded by rough walls is modeling the effect of surface roughness. Methods based on the mapping of the irregular boundary into a rectangular domain can provide very high accuracy. However, these methods suffer from two main disadvantages. The coefficient matrix associated with these methods is non-sparse type which consequently leads to a high

computational cost [16]. This draw back becomes prominent for unsteady problems as the coefficient matrix is reconstructed at each time step. Moreover, these algorithms have limitations in terms of geometry as they cannot handle singularity in the mapping.

The immersed boundary (IB) method provides a general conceptual basis for developing efficient computational tools to solve flow problems involving complex boundary geometries. The original concept was proposed by Peskin [17] in the context of cardiac mechanics problems. The method works by discretizing the governing equations within a regular computational domain that surrounds the complex flow domain. Special procedures are then used to enforce the boundary conditions along the physical boundaries, immersed within the computational domain. The computational efficiency of this class of methods stems from the elimination of the cost of generating boundary conforming grids.

The essence of the IB method is to impose forcing at the edge of the computational domain so that the flow quantities evaluated along the edge of the physical domain assume values specified by the boundary conditions. Various implementations have been developed over the past few decades [18, 19] with the forcing applied in either a continuous or discrete manner. The majority of implementations apply low-order finite-difference, finite-volume or finite-element techniques for the spatial discretization [20-22] resulting in limited spatial accuracy. Some recent implementations employ spectral discretization to improve the solution accuracy although the complete solutions are nevertheless not spectrally accurate [23, 24].

A fully, spectrally-accurate version of the IB method, referred to as the Immersed Boundary Conditions (IBC) method was proposed in [25] for two-dimensional flow problems. The geometry of the physical boundaries is described by Fourier expansions which limits the applicability of the method to periodic domains. The method is nevertheless applicable to a very wide class of problems of physical interest. The discretization relies on two types of Fourier expansions, one for the field variables and one for the boundary conditions. The boundary relations responsible for the enforcement of boundary conditions are constructed formally and provide the means to enforce these

conditions with spectral accuracy. Use of the Chebyshev expansions in the non-periodic direction makes the algorithm effectively gridless and, thus, allows quick adaptation to different geometries. The IBC method has been extended to unsteady problems involving both fixed [16] and time-dependent boundary shapes [26-29]. It has also been extended to three-dimensional problems described by the Laplace operator [30]. From an application perspective, the method has been instrumental in the search for drag reducing grooves [14, 15 and 31] as well as in the analysis of instabilities of shear layers bounded by grooved surfaces [32-38].

The construction of the boundary relations yields a number of constraints in the IBC method in excess of what is required to form a closed system of algebraic equations [39]. The “classical” formulation retains enough of these constraints corresponding to the lowest Fourier modes to form a closed system. Although spatial discretizations using Fourier and Chebyshev expansions lead to the coveted spectral convergence properties, the computational cost of the method increases very rapidly with increasing boundary complexities. This cost may be lowered by using the over-determined formulation where the number of boundary relations is in excess of the field equations [39]. The cost can also be lowered by using specialized linear solvers [40, 41].

The above discussion shows that most of the existing efforts, with the exception of [30], have been focused on two-dimensional problems. There is therefore a need to develop an extension of the IBC method suitable for the analysis of three-dimensional flows. One needs to pay attention to the memory and computational cost as both of them increase rapidly with increased geometric complexity. This is so because the modal equations resulting from the discretization of the field equation are coupled through boundary properties, unlike the case of a smooth channel [42].

The present work deals with the development of the three-dimensional version of the IBC method with applications focused on the analysis of flows in domains bounded by rough walls. Section 2 introduces the model problem. Section 3 describes the numerical formulation of the problem. In particular, Section 3.1 discusses the velocity-vorticity formulation and Section 3.2 presents the numerical discretization. Here, Section 3.2.1

presents the discretization of the field equations, Section 3.2.2 discusses the discretization of the boundary conditions and Section 3.2.3 presents the discretization of the flow constraints. Section 4 is focused on the solution process. In particular, Section 4.1 describes the specialized linear solver used repeatedly during the iterative solution process while Section 4.2 discusses efficiencies resulting from taking advantage of the complex conjugate property of the unknowns. Section 5 discusses the evaluation of the pressure field. Section 6 discusses testing of the algorithm. Section 7 presents the over-determined formulation of this algorithm and discusses the range of its applicability. Section 8 provides a short summary of the main conclusions

Section 2

2 Problem Formulation

The mathematical formulation of the problem has been presented in this section. Section 2.1 describes the geometry of flow domain, section 2.2 provides the governing equations, the reference flow has been introduced in section 2.3 and section 2.4 presents the flow between rough walls.

2.1 Geometry of the Flow Domain

Consider a channel formed by rough walls extending to $\pm\infty$ in the x - and z -directions. The upper and lower walls are located at $y_U(x, z)$ and $y_L(x, z)$, respectively. It is assumed that the roughness is periodic in the x - and z -directions with wavelengths $\lambda_x = 2\pi/\alpha$ and $\lambda_z = 2\pi/\beta$ where α and β stand for the wave numbers in the x - and z -directions, respectively (Figure 1). The channel geometry can be described using Fourier expansions of the form

$$y_U(x, z) = 1 + \sum_{n=-N_A}^{N_A} \sum_{m=-M_A}^{M_A} H_U^{(n,m)} e^{i(n\alpha x + m\beta z)}, \quad (2.1a)$$

$$y_L(x, z) = -1 + \sum_{n=-N_A}^{N_A} \sum_{m=-M_A}^{M_A} H_L^{(n,m)} e^{i(n\alpha x + m\beta z)} \quad (2.1b)$$

where half of the mean channel opening L has been used as the length scale and N_A and M_A denote the number of Fourier modes required for the description of the roughness geometry in the x - and z -directions. The expansion coefficients satisfy the reality conditions of the form $H_U^{(n,m)} = H_U^{(-n,-m)*}$, $H_U^{(n,-m)} = H_U^{(-n,m)*}$, $H_L^{(n,m)} = H_L^{(-n,-m)*}$ and $H_L^{(n,-m)} = H_L^{(-n,m)*}$ where star denotes the complex conjugates. As we are interested in the effect of flow modulations, we assume that the mean openings of the rough channel and the reference smooth channel are the same and, thus,

$$H_U^{(0,0)} = 0, H_M^{(0,0)} = 0. \quad (2.2)$$

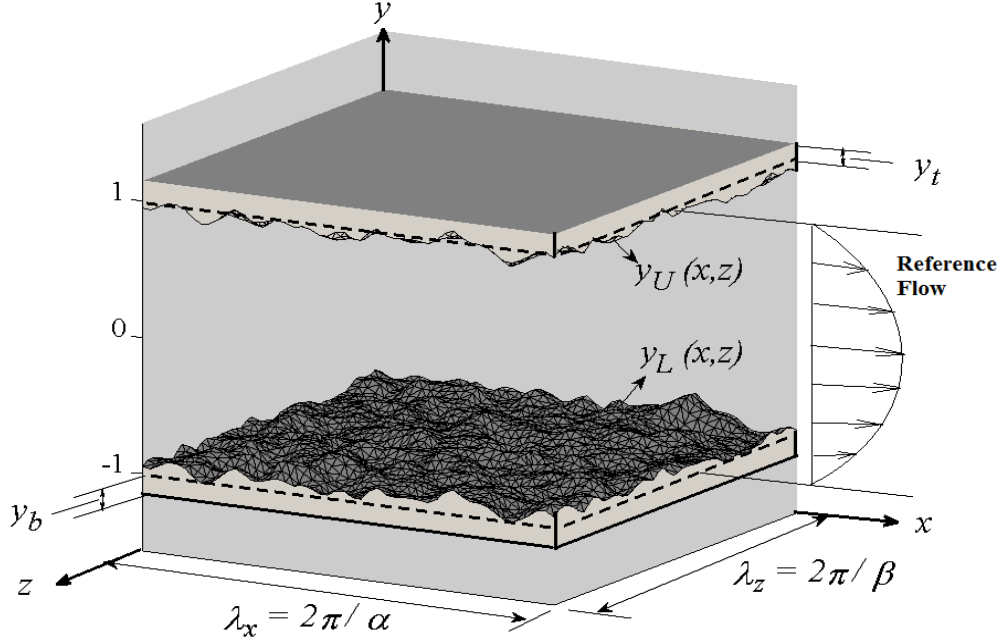


Figure 1: Sketch of the flow and computational domain.

2.2 Governing Equations

Flow in the channel is driven by a pressure gradient parallel to the (x, z) -plane. The velocity and pressure fields are described by the continuity and Navier-Stokes equations of the form

$$\nabla \cdot \vec{V} = 0, \quad (2.3a)$$

$$(\vec{V} \cdot \nabla) \vec{V} = -\nabla p + \frac{1}{Re} \nabla^2 \vec{V} \quad (2.3b)$$

where $\nabla = \left(\frac{\partial}{\partial x}, \frac{\partial}{\partial y}, \frac{\partial}{\partial z} \right)$, $\vec{V} = (u, v, w)$ is the velocity vector with u , v , w denoting components in the x -, y -, and z -directions, respectively, $\vec{V} \cdot \nabla = \left(u \frac{\partial}{\partial x} + v \frac{\partial}{\partial y} + w \frac{\partial}{\partial z} \right)$, and p stands for the pressure. In the above, U_{max} and ρU_{max}^2 have been used at the velocity and the pressure scales with ρ standing for the density. The proper choice of U_{max} is

discussed in Section 2.3. The Reynolds number Re is defined as LU_{max}/ν where ν denotes the kinematic viscosity.

The flow is subject to the no-slip and no-penetration conditions at the walls of the form

$$\vec{V} = 0 \text{ at } y = y_U(x, z) \text{ and } y = y_L(x, z). \quad (2.4)$$

2.3 Flow in a Smooth Channel

Flow in the smooth channel represents the reference case and the corresponding velocity and pressure field have the form

$$\vec{V}_0 = (u_0, v_0, w_0) = \left[\frac{Re}{2} e_x (1 - y^2), 0, \frac{Re}{2} e_z (1 - y^2) \right], \quad (2.5a)$$

$$p_0 = -e_x x - e_z z + c \quad (2.5b)$$

where $\vec{V}_0 = (u_0, v_0, w_0)$ is the reference velocity vector, p_0 stands for the reference pressure and e_x and e_z denote the pressure gradient components in the x - and z -directions, respectively. The total pressure gradient and its components are related according to the following relation

$$\sqrt{e_x^2 + e_z^2} = \frac{2}{Re}. \quad (2.6)$$

As the fluid flows in the direction of the total pressure gradient, one can choose either the x - or z -axis to coincide with this direction without loss of generality. The velocity scale U_{max} is chosen as the maximum of the velocity of the reference flow in the direction of the total pressure gradient.

2.4 Flow between Rough Walls

We shall represent flow between the rough walls as a sum of the reference flow and flow modifications due to the roughness. The total velocity and pressure field are expressed as

$$\begin{aligned}\vec{V}(x, y, z) &= (u(x, y, z), v(x, y, z), w(x, y, z)) \\ &= (u_0(y) + u_1(x, y, z), v_1(x, y, z), w_0(y) + w_1(x, y, z)),\end{aligned}\quad (2.7a)$$

$$p(x, y, z) = p_0(x, z) + p_1(x, y, z) = -e_x x - e_z z + e'_x x + e'_z z + p'(x, y, z) + c \quad (2.7b)$$

where subscripts 0 and 1 refer to the reference flow and the flow modification, respectively, e'_x and e'_z denote the modifications of the mean pressure gradient in the x - and z -directions, respectively, and $p'(x, y, z)$ denotes the periodic part of the pressure modifications.

Substitution of (2.7) into (2.3) yields the following form of the field equations

$$\frac{\partial u_1}{\partial x} + \frac{\partial v_1}{\partial y} + \frac{\partial w_1}{\partial z} = 0, \quad (2.8a)$$

$$\begin{aligned}u_0 \frac{\partial u_1}{\partial x} + v_0 \frac{\partial u_0}{\partial y} + w_0 \frac{\partial u_1}{\partial z} + \left(u_1 \frac{\partial u_1}{\partial x} + v_1 \frac{\partial u_1}{\partial y} + w_1 \frac{\partial u_1}{\partial z} \right) = \\ -\frac{\partial p_1}{\partial x} + \frac{1}{Re} \left(\frac{\partial^2 u_1}{\partial x^2} + \frac{\partial^2 u_1}{\partial y^2} + \frac{\partial^2 u_1}{\partial z^2} \right),\end{aligned}\quad (2.8b)$$

$$u_0 \frac{\partial v_1}{\partial x} + w_0 \frac{\partial v_1}{\partial z} + \left(u_1 \frac{\partial v_1}{\partial x} + v_1 \frac{\partial v_1}{\partial y} + w_1 \frac{\partial v_1}{\partial z} \right) = -\frac{\partial p_1}{\partial y} + \frac{1}{Re} \left(\frac{\partial^2 v_1}{\partial x^2} + \frac{\partial^2 v_1}{\partial y^2} + \frac{\partial^2 v_1}{\partial z^2} \right), \quad (2.8c)$$

$$\begin{aligned}u_0 \frac{\partial w_1}{\partial x} + v_1 \frac{\partial w_0}{\partial y} + w_0 \frac{\partial w_1}{\partial z} + \left(u_1 \frac{\partial w_1}{\partial x} + v_1 \frac{\partial w_1}{\partial y} + w_1 \frac{\partial w_1}{\partial z} \right) = \\ -\frac{\partial p_1}{\partial z} + \frac{1}{Re} \left(\frac{\partial^2 w_1}{\partial x^2} + \frac{\partial^2 w_1}{\partial y^2} + \frac{\partial^2 w_1}{\partial z^2} \right).\end{aligned}\quad (2.8d)$$

The boundary conditions (2.4) can be expressed in the form

$$u_1(y_U(x, z)) = -u_0(y_U(x, z)), \quad (2.9a)$$

$$u_1(y_L(x, z)) = -u_0(y_L(x, z)), \quad (2.9b)$$

$$v_1(y_U(x, z)) = 0, \quad (2.9c)$$

$$v_1(y_L(x, z)) = 0, \quad (2.9d)$$

$$w_1(y_U(x, z)) = -w_0(y_U(x, z)), \quad (2.9e)$$

$$w_1(y_L(x, z)) = -w_0(y_L(x, z)). \quad (2.9f)$$

The above system needs two closing conditions. We shall consider either the fixed flow rate constraint or the fixed pressure gradient constraint in both the x - and z -directions. To apply the fixed flow rate constraint we assume that the mean flow rates in x - and z -directions are known. This constraint in the x -direction takes the form of

$$\begin{aligned} Q(x)|_{mean} &= \frac{1}{2\pi/\beta} \int_0^{2\pi/\beta} \int_{y_L(x,z)}^{y_U(x,z)} u(x, y, z) dy dz \\ &= \frac{1}{2\pi/\beta} \int_0^{2\pi/\beta} \int_{y_L(x,z)}^{y_U(x,z)} [u_0(y) + u_1(x, y, z)] dy dz \\ &= Q_{x0} + Q_{x1} \end{aligned} \quad (2.10)$$

where Q_{x0} and Q_{x1} are the reference flow rate and the flow rate modification due to roughness, respectively. Q_{x1} can be specified arbitrarily with $Q_{x1} = 0$ implying that the flow rates in the smooth and rough channels are the same. The flow rate constraint in the z -direction can be specified in a similar manner and involves Q_{z0} and Q_{z1} .

The fixed pressure gradient constraints correspond to the specification of the mean pressure gradients in both the x - and z -directions. The mean pressure gradient in the x -direction can be expressed as

$$\partial_x p|_{mean} = -e_x + e'_x \quad (2.11)$$

where e_x and e'_x refers to the pressure gradient of the reference flow and the roughness induced modification, respectively. e'_x can be selected arbitrarily with $e'_x = 0$ implying that flows in the smooth and rough channels are driven by the same pressure gradient. The pressure gradient constraint in the z -direction can be specified in a similar manner and involves e_z and e'_z .

Section 3

3 Numerical Solution of the Problem

This section contains the numerical solution of the flow problem. Section 3.1 provides the suitable form of the governing equations for numerical solution. Section 3.1 deals with the numerical discretization of the problem where, 3.2.1 presents the discretization of the field equations, section 3.2.2 discusses the discretization of the boundary conditions and section 3.2.3 presents the discretization of the fixed flow rate constraint.

3.1 Forms of the Governing Equations Suitable for the Numerical Solution

We shall use the velocity-vorticity formulation. The vorticity vector is defined as

$$\vec{\omega}(x, y, z) = \nabla \times \vec{V} = (\omega_x(x, y, z), \omega_y(x, y, z), \omega_z(x, y, z)) = \vec{\omega}_0(y) + \vec{\omega}_1(x, y, z), \quad (3.1)$$

where

$$\vec{\omega}_0 = (-e_z Re y, 0, e_x Re y), \quad (3.2a)$$

$$\vec{\omega}_1 = (\xi_1, \eta_1, \zeta_1) = \left(\frac{\partial w_1}{\partial y} - \frac{\partial v_1}{\partial z}, \frac{\partial u_1}{\partial z} - \frac{\partial w_1}{\partial x}, \frac{\partial v_1}{\partial x} - \frac{\partial u_1}{\partial y} \right). \quad (3.2b)$$

In the above, $\vec{\omega}_0$ stands for the vorticity of the reference flow and $\vec{\omega}_1$ denotes the vorticity modifications. The field equations can be reduced to a system of two equations for the wall-normal vorticity and velocity components, i.e. for η_1 and v_1 , in the form of

$$-\frac{1}{Re} \nabla^2 (\nabla^2 v_1) + \left(u_0 \frac{\partial}{\partial x} + w_0 \frac{\partial}{\partial z} \right) (\nabla^2 v_1) - \frac{\partial^2 u_0}{\partial y^2} \frac{\partial v_1}{\partial x} - \frac{\partial^2 w_0}{\partial y^2} \frac{\partial v_1}{\partial z} = N_v, \quad (3.3a)$$

$$-\frac{1}{Re} \nabla^2 \eta_1 + u_0 \frac{\partial \eta_1}{\partial x} + w_0 \frac{\partial \eta_1}{\partial z} + \frac{\partial v_1}{\partial z} \frac{\partial u_0}{\partial y} - \frac{\partial v_1}{\partial x} \frac{\partial w_0}{\partial y} = N_\eta \quad (3.3b)$$

where

$$N_\eta = \frac{\partial H_w}{\partial x} - \frac{\partial H_u}{\partial z}, \quad (3.4a)$$

$$N_v = \frac{\partial}{\partial y} \left(\frac{\partial H_u}{\partial x} + \frac{\partial H_w}{\partial z} \right) - \left(\frac{\partial^2}{\partial x^2} + \frac{\partial^2}{\partial z^2} \right) H_v, \quad (3.4b)$$

$$H_u = u_1 \frac{\partial u_1}{\partial x} + v_1 \frac{\partial u_1}{\partial y} + w_1 \frac{\partial u_1}{\partial z} = \frac{\partial}{\partial x}(u_1 u_1) + \frac{\partial}{\partial y}(u_1 v_1) + \frac{\partial}{\partial z}(u_1 w_1), \quad (3.4c)$$

$$H_v = u_1 \frac{\partial v_1}{\partial x} + v_1 \frac{\partial v_1}{\partial y} + w_1 \frac{\partial v_1}{\partial z} = \frac{\partial}{\partial x}(u_1 v_1) + \frac{\partial}{\partial y}(v_1 v_1) + \frac{\partial}{\partial z}(v_1 w_1), \quad (3.4d)$$

$$H_w = u_1 \frac{\partial w_1}{\partial x} + v_1 \frac{\partial w_1}{\partial y} + w_1 \frac{\partial w_1}{\partial z} = \frac{\partial}{\partial x}(u_1 w_1) + \frac{\partial}{\partial y}(v_1 w_1) + \frac{\partial}{\partial z}(w_1 w_1). \quad (3.4e)$$

The nonlinear terms have been placed on the right hand sides as these terms are considered known during the iterative solution process. The solution of (3.3) provides η_1 and v_1 while u_1 and w_1 are determined from the continuity equation and the definition of the wall-normal vorticity by solving the following system

$$\left(\frac{\partial^2}{\partial x^2} + \frac{\partial^2}{\partial z^2} \right) u_1 = - \frac{\partial^2 v_1}{\partial x \partial y} + \frac{\partial \eta_1}{\partial z}, \quad (3.5a)$$

$$\left(\frac{\partial^2}{\partial x^2} + \frac{\partial^2}{\partial z^2} \right) w_1 = - \left(\frac{\partial^2 v_1}{\partial x \partial y} + \frac{\partial \eta_1}{\partial z} \right). \quad (3.5b)$$

The appropriate form of the boundary conditions expressed in terms of η_1 and v_1 will be presented later in the text.

The above formulation has two limiting cases. Surface roughness in the form of transverse grooves results in two-dimensional flow modifications. In this case the vorticity equation (3.3b) is identically satisfied and the wall normal vorticity becomes zero. The velocity equation (3.3a) reduces to

$$-\frac{1}{Re} \nabla^2 (\nabla^2 v_1) + u_0 \frac{\partial}{\partial x} (\nabla^2 v_1) - \frac{\partial^2 u_0}{\partial y^2} \frac{\partial v_1}{\partial x} = \frac{\partial}{\partial y} \left(\frac{\partial H_u}{\partial x} \right) - \frac{\partial^2}{\partial x} H_v \quad (3.6)$$

which is equivalent to the equation studied in [42]. When the roughness has the form of longitudinal grooves, the flow modifications are independent of the direction of the reference flow, the normal and spanwise velocity modifications disappear, the velocity equation (3.3a) is identically satisfied and the vorticity equation reduces to the form

$$\frac{\partial}{\partial z} \left(\frac{\partial^2 u_1}{\partial y^2} + \frac{\partial^2 u_1}{\partial z^2} \right) = 0 \quad (3.7)$$

which is equivalent to the x -momentum equation simplified for such flow configurations and studied in [14].

In the present case, the wall-normal velocity and vorticity equations are solved as a system in both special cases and the properties of the limiting solutions are used for verification of the consistency of the algorithm.

3.2 Discretization Method

We wish to determine the solution of the flow problem presented in the previous section with spectral accuracy. We shall use the Immersed Boundary Conditions (IBC) concept in order to deal with the irregularity of the solution domain. We select a fixed rectangular computational domain extending over one period in the x - and z -directions and extending in the y -direction in such a way that the rough boundaries are completely submerged inside the computational domain and replace the flow boundary conditions with the equivalent boundary constraints. Figure 1 illustrates the form of the computational domain. We shall use Chebyshev polynomials for discretization in the transverse direction and, in order to use their standard definition, the y -extent of the computational domain needs to be mapped into $[-1, 1]$. A mapping of the form

$$\hat{y} = \Gamma[y - (1 + y_t)] + 1 \quad (3.8)$$

is used where $\hat{y} \in [-1, 1]$, $\Gamma = 2/(2 + y_t + y_b)$, and y_t and y_b stand for the locations of extremities of the upper and lower walls (see Fig.1), respectively.

The wall geometries are expressed in the new coordinate system in the form of

$$\hat{y}_U = \sum_{n=-N_A}^{N_A} \sum_{m=-M_A}^{M_A} A_U^{(n,m)} e^{i(nax+m\beta z)}, \quad (3.9a)$$

$$\hat{y}_L = \sum_{n=-N_A}^{N_A} \sum_{m=-M_A}^{M_A} A_L^{(n,m)} e^{i(nax+m\beta z)} \quad (3.9b)$$

where

$$A_U^{(0,0)} = 1 + \Gamma[-y_t + H_U^{(0,0)}], \quad A_U^{(n,m)} = \Gamma H_U^{(n,m)} \text{ for } (n, m) \neq (0,0), \quad (3.10a)$$

$$A_L^{(0,0)} = 1 + \Gamma \left[-(2 + y_t) + H_L^{(0,0)} \right], A_L^{(n,m)} = \Gamma H_L^{(n,m)} \text{ for } (n, m) \neq (0,0). \quad (3.10b)$$

The governing equations transform to the following form

$$-\frac{1}{Re} \left(\frac{\partial^2}{\partial x^2} + \Gamma^2 \frac{\partial^2}{\partial \hat{y}^2} + \frac{\partial^2}{\partial z^2} \right)^2 v_1 + \left(u_0 \frac{\partial}{\partial x} + w_0 \frac{\partial}{\partial z} \right) \left(\frac{\partial^2}{\partial x^2} + \Gamma^2 \frac{\partial^2}{\partial \hat{y}^2} \right) v_1 - \Gamma^2 \frac{\partial^2 u_0}{\partial \hat{y}^2} \frac{\partial v_1}{\partial x} - \Gamma^2 \frac{\partial^2 w_0}{\partial \hat{y}^2} \frac{\partial v_1}{\partial z} = N_v, \quad (3.11a)$$

$$-\frac{1}{Re} \left(\frac{\partial^2}{\partial x^2} + \Gamma^2 \frac{\partial^2}{\partial \hat{y}^2} + \frac{\partial^2}{\partial z^2} \right) \eta_1 + u_0 \frac{\partial \eta_1}{\partial x} + w_0 \frac{\partial \eta_1}{\partial z} + \Gamma \frac{\partial v_1}{\partial z} \frac{\partial u_0}{\partial \hat{y}} - \Gamma \frac{\partial v_1}{\partial x} \frac{\partial w_0}{\partial \hat{y}} = N_\eta \quad (3.11b)$$

where

$$N_\eta = \frac{\partial H_w}{\partial x} - \frac{\partial H_u}{\partial z}, \quad (3.12a)$$

$$N_v = \frac{\partial}{\partial x} \left(\frac{\partial H_u}{\partial x} + \frac{\partial H_w}{\partial z} \right) - \left(\frac{\partial^2}{\partial x^2} + \frac{\partial^2}{\partial z^2} \right) H_v, \quad (3.12b)$$

$$H_u = \frac{\partial}{\partial x} (u_1 u_1) + \Gamma \frac{\partial}{\partial \hat{y}} (u_1 v_1) + \frac{\partial}{\partial z} (u_1 w_1), \quad (3.12c)$$

$$H_v = \frac{\partial}{\partial x} (u_1 v_1) + \Gamma \frac{\partial}{\partial \hat{y}} (v_1 v_1) + \frac{\partial}{\partial z} (v_1 w_1), \quad (3.12d)$$

$$H_w = \frac{\partial}{\partial x} (u_1 w_1) + \Gamma \frac{\partial}{\partial \hat{y}} (v_1 w_1) + \frac{\partial}{\partial z} (w_1 w_1). \quad (3.12e)$$

The fixed flow rate constraint in the new coordinate system is expressed as follows

$$Q(x)|_{mean} = \frac{1}{2\pi/\beta} \int_0^{2\pi/\beta} \int_{\hat{y}_L(x,z)}^{\hat{y}_U(x,z)} \left[\frac{1}{\Gamma} u_0(\hat{y}) + \frac{1}{\Gamma} u_1(x, \hat{y}, z) \right] d\hat{y} dz = Q_{x0} + Q_{x1} \quad (3.13)$$

while the form of the fixed pressure gradient constraint remains unchanged, i.e. it is given by (2.11).

3.2.1 Discretization of the Field Equations

The unknowns are represented as Fourier expansions in the periodic directions of the form

$$\begin{aligned}\eta_1(x, \hat{y}, z) &= \sum_{n=-\infty}^{\infty} \sum_{m=-\infty}^{\infty} \eta^{(n,m)}(\hat{y}) e^{i(n\alpha x + m\beta z)} \\ &\approx \sum_{n=-N_M}^{N_M} \sum_{m=-M_M}^{M_M} \eta^{(n,m)}(\hat{y}) e^{i(n\alpha x + m\beta z)},\end{aligned}\quad (3.14a)$$

$$\begin{aligned}u_1(x, \hat{y}, z) &= \sum_{n=-\infty}^{\infty} \sum_{m=-\infty}^{\infty} u^{(n,m)}(\hat{y}) e^{i(n\alpha x + m\beta z)} \\ &\approx \sum_{n=-N_M}^{N_M} \sum_{m=-M_M}^{M_M} u^{(n,m)}(\hat{y}) e^{i(n\alpha x + m\beta z)},\end{aligned}\quad (3.14b)$$

$$\begin{aligned}v_1(x, \hat{y}, z) &= \sum_{n=-\infty}^{\infty} \sum_{m=-\infty}^{\infty} v^{(n,m)}(\hat{y}) e^{i(n\alpha x + m\beta z)} \\ &\approx \sum_{n=-N_M}^{N_M} \sum_{m=-M_M}^{M_M} v^{(n,m)}(\hat{y}) e^{i(n\alpha x + m\beta z)},\end{aligned}\quad (3.14c)$$

$$\begin{aligned}w_1(x, \hat{y}, z) &= \sum_{n=-\infty}^{\infty} \sum_{m=-\infty}^{\infty} w^{(n,m)}(\hat{y}) e^{i(n\alpha x + m\beta z)} \\ &\approx \sum_{n=-N_M}^{N_M} \sum_{m=-M_M}^{M_M} w^{(n,m)}(\hat{y}) e^{i(n\alpha x + m\beta z)}\end{aligned}\quad (3.14d)$$

where N_M and M_M represent truncations in the x - and z -directions, respectively, and $\eta^{(n,m)}$, $u^{(n,m)}$, $v^{(n,m)}$, $w^{(n,m)}$ are the modal functions for the wall-normal vorticity and the streamwise, wall-normal and spanwise velocity components, respectively. The modal functions satisfy the reality conditions of the form $\eta^{(n,m)} = \eta^{(-n,-m)*}$, $\eta^{(n,-m)} = \eta^{(-n,m)*}$, $u^{(n,m)} = u^{(-n,-m)*}$, $u^{(n,-m)} = u^{(-n,m)*}$, $v^{(n,m)} = v^{(-n,-m)*}$, $v^{(n,-m)} = v^{(-n,m)*}$, $w^{(n,m)} = w^{(-n,-m)*}$, $w^{(n,-m)} = w^{(-n,m)*}$ where star denotes the complex conjugates.

Substitution of (3.14) into (3.11) and separation of Fourier modes lead to a system of ordinary differential equations for the modal function of the form

$$\begin{aligned}&\left[\frac{D_{nm}^2}{Re} + i\alpha(-u_0, D_{nm} + D^2 u_0) + im\beta(-w_0 D_{nm} + D^2 w_0) \right] v^{(n,m)}(\hat{y}) \\ &= -N_v^{(n,m)}\end{aligned}\quad (3.15a)$$

$$\begin{aligned} & \left(\frac{D_{nm}}{Re} - in\alpha u_0 - im\beta w_0 \right) \eta^{(n,m)}(\hat{y}) + (in\alpha D w_0 - im\beta D u_0) v^{(n,m)}(\hat{y}) \\ & = -N_\eta^{(n,m)} \end{aligned} \quad (3.15b)$$

for $-N_M \leq n \leq N_M$ and $-M_M \leq m \leq M_M$ where

$$D^q = \Gamma^q \frac{d^q}{dy^q}, \quad (3.16a)$$

$$D_{nm} = D^2 - k_{nm}^2, \quad (3.16b)$$

$$k_{nm}^2 = n^2 \alpha^2 + m^2 \beta^2, \quad (3.16c)$$

$$N_v^{(n,m)} = iD[n\alpha H_u^{(n,m)} + m\beta H_w^{(n,m)}] + k_{nm}^2 H_v^{(n,m)}, \quad (3.16d)$$

$$N_\eta^{(n,m)} = in\alpha H_w^{(n,m)} - im\beta H_u^{(n,m)}, \quad (3.16e)$$

$$H_u^{(n,m)} = in\alpha \langle u_1 u_1 \rangle^{(n,m)} + D \langle u_1 v_1 \rangle^{(n,m)} + im\beta \langle u_1 w_1 \rangle^{(n,m)}, \quad (3.16f)$$

$$H_v^{(n,m)} = in\alpha \langle u_1 v_1 \rangle^{(n,m)} + D \langle v_1 v_1 \rangle^{(n,m)} + im\beta \langle v_1 w_1 \rangle^{(n,m)}, \quad (3.16g)$$

$$H_w^{(n,m)} = in\alpha \langle u_1 w_1 \rangle^{(n,m)} + D \langle v_1 w_1 \rangle^{(n,m)} + im\beta \langle w_1 w_1 \rangle^{(n,m)}. \quad (3.16h)$$

In the above, $\langle u_1 u_1 \rangle^{(n,m)}$ denotes the Fourier coefficients of the product $(u_1 u_1)$, i.e.

$$(u_1 u_1) = \sum_{n=-\infty}^{\infty} \sum_{m=-\infty}^{\infty} \langle u_1 u_1 \rangle^{(n,m)}(\hat{y}) e^{i(n\alpha x + m\beta z)}. \quad (3.17)$$

Similar notation is used for the other products, i.e. $(u_1 v_1)$, $(u_1 w_1)$, $(v_1 v_1)$, $(v_1 w_1)$, $(w_1 w_1)$. Functions N_v , N_η , H_u , H_v , H_w , which are treated as known during the solution process, are replaced by their Fourier expansions with $N_v^{(n,m)}$, $N_\eta^{(n,m)}$, $H_u^{(n,m)}$, $H_v^{(n,m)}$, $H_w^{(n,m)}$ representing the relevant modal functions. Equation (3.15) represents a sixth-order sub-system for each modal function and requires six boundary conditions. Solution of the complete system results in the determination of the modal functions for v_1 and η_1 . The modal form of (3.5) provides expressions for the evaluation of the modal function for u_1 and w_1 , i.e.

$$u^{(n,m)}(\hat{y}) = \frac{1}{k_{nm}^2} [in\alpha Dv^{(n,m)} - im\beta\eta^{(n,m)}], \quad (3.18a)$$

$$w^{(n,m)}(\hat{y}) = \frac{1}{k_{nm}^2} [im\beta Dv^{(n,m)} + in\alpha\eta^{(n,m)}]. \quad (3.18b)$$

System (3.15) written for $n = m = 0$ leads to $v^{(0,0)} = 0$ and $\eta^{(0,0)} = 0$ (see Appendix A) and, thus, it does not provide a basis for the evaluation of both $u^{(0,0)}$ and $w^{(0,0)}$. As these two components contribute to the nonlinear terms, it is necessary to provide other means for their determination. Here we return to the primitive variables, substitute (3.14b)-(3.14d) into the x - and z -components of the momentum equation (2.3b) and extract modes $(n, m) = (0, 0)$ to arrive at

$$\frac{1}{Re} D^2 u^{(0,0)} = e'_x + D\langle u_1 v_1 \rangle^{(0,0)}, \quad (3.19a)$$

$$\frac{1}{Re} D^2 w^{(0,0)} = e'_z + D\langle v_1 w_1 \rangle^{(0,0)}. \quad (3.19b)$$

The above system is fourth-order, requires four boundary conditions and involves two unknown constants, i.e. e'_x and e'_z . For the fixed pressure gradient constraints, both e'_x and e'_z are specified. For the fixed flow rate constraint, the specified flow rate corrections Q_{x1} and Q_{z1} provide conditions required for the determination of e'_x and e'_z . We shall discuss the numerical implementation of these conditions later in this presentation.

The solution of the modal equations (3.15) and (3.19) begins with expressing the modal functions in terms of Chebyshev expansions of the form

$$\eta^{(n,m)}(\hat{y}) = \sum_{k=0}^{\infty} \eta_k^{(n,m)} T_k(\hat{y}) \approx \sum_{k=0}^{N_T-1} \eta_k^{(n,m)} T_k(\hat{y}), \quad (3.20a)$$

$$u^{(n,m)}(\hat{y}) = \sum_{k=0}^{\infty} u_k^{(n,m)} T_k(\hat{y}) \approx \sum_{k=0}^{N_T-1} u_k^{(n,m)} T_k(\hat{y}), \quad (3.20b)$$

$$v^{(n,m)}(\hat{y}) = \sum_{k=0}^{\infty} v_k^{(n,m)} T_k(\hat{y}) \approx \sum_{k=0}^{N_T-1} v_k^{(n,m)} T_k(\hat{y}), \quad (3.20c)$$

$$w^{(n,m)}(\hat{y}) = \sum_{k=0}^{\infty} w_k^{(n,m)} T_k(\hat{y}) \approx \sum_{k=0}^{N_T-1} w_k^{(n,m)} T_k(\hat{y}) \quad (3.20d)$$

where $\eta_k^{(n,m)}$, $u_k^{(n,m)}$, $v_k^{(n,m)}$ and $w_k^{(n,m)}$ are the Chebyshev expansion coefficients for the modal functions of $\eta^{(n,m)}$, $u^{(n,m)}$, $v^{(n,m)}$ and $w^{(n,m)}$, T_k denotes the k^{th} -order Chebyshev polynomial of the first kind and N_T is the number of Chebyshev polynomials retained in the solution.

Algebraic equations for the Chebyshev expansion coefficients are constructed using the Galerkin projection method. Equations (3.20) are substituted into (3.15) and (3.19), and projections of residua onto the base functions are set to zero. This process is explained using equation (3.15a) as an example and similar processes are used with the remaining equations.

Substitution of (3.20) into (3.15a) provides the following expression

$$\begin{aligned} \sum_{k=0}^{N_T-1} \left[\frac{1}{Re} D^4 T_k - \frac{2k_{nm}^2}{Re} D^2 T_k + \frac{k_{nm}^4}{Re} T_k - in\alpha u_0 D^2 T_k + in\alpha k_{nm}^2 u_0 T_k + in\alpha (D^2 u_0) T_k - \right. \\ \left. im\beta w_0 D^2 T_k + im\beta k_{nm}^2 w_0 T_k + im\beta (D^2 w_0) T_k \right] v_k^{(n,m)} = \\ \left[-in\alpha D^2 \langle u_1 v_1 \rangle^{(n,m)} - im\beta D^2 \langle v_1 w_1 \rangle^{(n,m)} \right] + \\ \left[(n\alpha)^2 D \langle u_1 u_1 \rangle^{(n,m)} + 2nm\alpha\beta D \langle u_1 w_1 \rangle^{(n,m)} + (m\beta)^2 D \langle w_1 w_1 \rangle^{(n,m)} - \right. \\ \left. k_{nm}^2 D \langle v_1 v_1 \rangle^{(n,m)} \right] + \left[-in\alpha k_{nm}^2 \langle u_1 v_1 \rangle^{(n,m)} - im\beta k_{nm}^2 \langle v_1 w_1 \rangle^{(n,m)} \right] \end{aligned} \quad (3.21)$$

where $N_v^{(n,m)}$ on the right hand side is written in an explicit manner. All terms on the right hand side are considered to be known and need to be expressed in terms of Chebyshev expansions as follows

$$\begin{aligned} \left[\langle u_1 u_1 \rangle^{(n,m)}, \langle u_1 v_1 \rangle^{(n,m)}, \langle u_1 w_1 \rangle^{(n,m)}, \langle v_1 v_1 \rangle^{(n,m)}, \langle v_1 w_1 \rangle^{(n,m)}, \langle w_1 w_1 \rangle^{(n,m)} \right] (\hat{y}) = \\ \sum_{k=0}^{N_T-1} \left[(G_{uu})_k^{(n,m)}, (G_{uv})_k^{(n,m)}, (G_{uw})_k^{(n,m)}, (G_{vv})_k^{(n,m)}, (G_{vw})_k^{(n,m)}, (G_{ww})_k^{(n,m)} \right] T_k(\hat{y}) \end{aligned} \quad (3.22)$$

where $(G_{uu})_k^{(n,m)}, (G_{uv})_k^{(n,m)}, (G_{uw})_k^{(n,m)}, (G_{vv})_k^{(n,m)}, (G_{vw})_k^{(n,m)}, (G_{ww})_k^{(n,m)}$ are expansion coefficients for the modal functions of the relevant products, e.g. $(G_{uu})_k^{(n,m)}$ is

the k -th expansion coefficient for the modal function (m, n) of the product $(u_1 u_1)$. These coefficients need to be recomputed at the beginning of each iteration with the relevant method described in Appendix B.

Substitution of (3.22) into (3.21) provides the following expression for the residue function

$$\begin{aligned} & \sum_{k=0}^{N_T-1} \left[\frac{1}{Re} D^4 T_k - \frac{2k_{nm}^2}{Re} D^2 T_k + \frac{k_{nm}^4}{Re} T_k - in\alpha u_0 D^2 T_k + in\alpha k_{nm}^2 u_0 T_k + in\alpha (D^2 u_0) T_k - \right. \\ & \left. im\beta w_0 D^2 T_k + im\beta k_{nm}^2 w_0 T_k + im\beta (D^2 w_0) T_k \right] v_k^{(n,m)} - \sum_{k=0}^{N_T-1} \left\{ [-in\alpha (G_{uv})_k^{(n,m)} - \right. \\ & \left. im\beta (G_{vw})_k^{(n,m)}] D^2 T_k + [n^2 \alpha^2 (G_{uu})_k^{(n,m)} + 2nm\alpha\beta (G_{uw})_k^{(n,m)} + m^2 \beta^2 (G_{ww})_k^{(n,m)} - \right. \\ & \left. k_{nm}^2 (G_{vv})_k^{(n,m)}] DT_k + [-in\alpha k_{nm}^2 (G_{uv})_k^{(n,m)} - im\beta k_{nm}^2 (G_{vw})_k^{(n,m)}] T_k \right\} = Residue(\hat{y}). \end{aligned} \quad (3.23)$$

Its projections onto the base functions are expressed in terms of the inner product defined as

$$\langle Residue(\hat{y}), T_j(\hat{y}) \rangle = \int_{\hat{y}=-1}^{\hat{y}=1} Residue(\hat{y}) T_j(\hat{y}) \omega(\hat{y}) d\hat{y} \quad (3.24)$$

where $\omega = 1/\sqrt{1-\hat{y}^2}$ is the weight function. Equation (3.24) can be written explicitly as

$$\begin{aligned} & \sum_{k=0}^{N_T-1} \left[\frac{1}{Re} \langle T_j, D^4 T_k \rangle - \frac{2k_{nm}^2}{Re} \langle T_j, D^2 T_k \rangle + \frac{k_{nm}^4}{Re} \langle T_j, T_k \rangle - in\alpha \langle T_j, u_0 D^2 T_k \rangle + \right. \\ & \left. in\alpha k_{nm}^2 \langle T_j, u_0 T_k \rangle + in\alpha \langle T_j, D^2 u_0 T_k \rangle - im\beta \langle T_j, w_0 D^2 T_k \rangle + im\beta k_{nm}^2 \langle T_j, w_0 T_k \rangle + \right. \\ & \left. im\beta \langle T_j, D^2 w_0 T_k \rangle \right] v_k^{(n,m)} = \sum_{k=0}^{N_T-1} \left\{ [-in\alpha (G_{uv})_k^{(n,m)} - im\beta (G_{vw})_k^{(n,m)}] \langle T_j, D^2 T_k \rangle + \right. \\ & \left[n^2 \alpha^2 (G_{uu})_k^{(n,m)} + 2nm\alpha\beta (G_{uw})_k^{(n,m)} + m^2 \beta^2 (G_{ww})_k^{(n,m)} - k_{nm}^2 (G_{vv})_k^{(n,m)} \right] \langle T_j, DT_k \rangle + \\ & \left. [-in\alpha k_{nm}^2 (G_{uv})_k^{(n,m)} - im\beta k_{nm}^2 (G_{vw})_k^{(n,m)}] \langle T_j, T_k \rangle \right\}, \quad 0 \leq j \leq N_T - 5 \end{aligned} \quad (3.25a)$$

where $-N_M \leq n \leq N_M$, $-M_M \leq m \leq M_M$ with $(n, m) \neq (0, 0)$. This process results in N_T equations for each modal function, however, we shall retain only the first $N_T - 4$ equations in order to make space for the boundary relations (tau method).

A similar process applied to (3.15b) results in

$$\begin{aligned} & \sum_{k=0}^{N_T-1} \left[\left(\frac{1}{Re} \langle T_j, D^2 T_k \rangle - \frac{k_{\hat{n}}^2 m}{Re} \langle T_j, T_k \rangle - in\alpha \langle T_j, u_0 T_k \rangle - im\beta \langle T_j, w_0 T_k \rangle \right) \eta_k^{(n,m)} + \right. \\ & \left. (in\alpha \langle T_j, Dw_0 T_k \rangle - im\beta \langle T_j, Du_0 T_k \rangle) v_k^{(n,m)} \right] = \\ & \sum_{k=0}^{N_T-1} \left\{ \left[-in\alpha (G_{vw})_k^{(n,m)} + im\beta (G_{uv})_k^{(n,m)} \right] \langle T_j, DT_k \rangle + \left[(n^2 \alpha^2 - m^2 \beta^2) (G_{uw})_k^{(n,m)} + \right. \right. \\ & \left. \left. nm\alpha\beta (G_{ww})_k^{(n,m)} - nm\alpha\beta (G_{uv})_k^{(n,m)} \right] \right\}, \quad 0 \leq j \leq N_T - 3 \end{aligned} \quad (3.25b)$$

where we retain only $N_T - 2$ leading equations, and applied to (3.19) leads to

$$\begin{aligned} \frac{1}{Re} \sum_{k=0}^{N_T-1} u_k^{(0,0)} \langle T_j, D^2 T_k \rangle &= e'_x \langle T_j, T_0 \rangle + \sum_{k=0}^{N_T} (G_{uv})_k^{(0,0)} \langle T_j, DT_k \rangle, \\ & 0 \leq j \leq N_T - 3, \end{aligned} \quad (3.26a)$$

$$\begin{aligned} \frac{1}{Re} \sum_{k=0}^{N_T-1} w_k^{(0,0)} \langle T_j, D^2 T_k \rangle &= e'_z \langle T_j, T_0 \rangle + \sum_{k=0}^{N_T} (G_{vw})_k^{(0,0)} \langle T_j, DT_k \rangle, \\ & 0 \leq j \leq N_T - 3, \end{aligned} \quad (3.26b)$$

where we also retain only $N_T - 2$ of the leading equations. The inner products of the Chebyshev polynomials found in (3.25)-(3.26) are given analytically in the form of

$$\langle T_j, T_k \rangle = \begin{cases} 0 & \text{for } j \neq k, \\ \pi & \text{for } j = k = 0, \\ \pi/2 & \text{for } j = k > 0. \end{cases} \quad (3.27)$$

The inner products involving the derivatives of the Chebyshev polynomials can be expressed analytically with the help of the following relations

$$T_0(\hat{y}) = 1, \quad T_1(\hat{y}) = \hat{y}, \quad T_{k+1}(\hat{y}) = 2\hat{y}T_k(\hat{y}) - T_{k-1}(\hat{y}) \quad (3.28)$$

$$D^n T_0(\hat{y}) = 0 \text{ for } n \geq 1, \quad DT_1(\hat{y}) = 1, \quad D^n T_1(\hat{y}) = 0 \text{ for } n \geq 2 \quad (3.29)$$

$$D^n T_{k+1}(\hat{y}) = 2nD^{n-1}T_k(\hat{y}) + 2\hat{y}D^n T_k(\hat{y}) - D^n T_{k-1}(\hat{y}) \text{ for } n \geq 1 \quad (3.30)$$

Evaluation of the inner products involving the reference flow quantities is explained using $\langle T_j, u_0 T_k \rangle$ as an example. $u_0(\hat{y})$ is expressed in terms of the Chebyshev expansion of the form

$$u_0(\hat{y}) = \sum_{m=0}^M U_m T_m(\hat{y}), \quad (3.31)$$

where U_m stands for the expansion coefficients. According to (2.5) and (3.8), $u_0(\hat{y})$ can also be expressed as

$$u_0(\hat{y}) = \frac{2}{Re} e_x (-a\hat{y}^2 - 2ab\hat{y} + 1 - b^2) \quad (3.32)$$

where, $a = \Gamma^{-1}$ and $b = -\Gamma^{-1} + 1 + y_t$. Comparison of (3.31) and (3.32) results in

$$U_0 = \frac{2}{Re} e_x \left(1 - \frac{a^2}{2} - b^2\right), U_1 = -\frac{4ab}{Re} e_x, U_2 = -\frac{a^2 e_x}{Re}. \quad (3.33)$$

The inner product $\langle T_j, u_0 T_k \rangle$ can be written as

$$\langle T_j, u_0 T_k \rangle = \int_{\hat{y}=-1}^{\hat{y}=1} \sum_{m=0}^2 T_j U_m T_m T_k \omega d\hat{y} = \sum_{m=0}^2 U_m \int_{\hat{y}=-1}^{\hat{y}=1} T_j T_m T_k \omega d\hat{y} \quad (3.34)$$

Since a product of two Chebyshev polynomials can be expressed as a sum of the form

$$T_j T_m = \frac{1}{2} (T_{j+m} + T_{|j-m|}), \quad (3.35)$$

(3.34) can be expressed as

$$\begin{aligned} \langle T_j, u_0 T_k \rangle &= \frac{1}{2} \sum_{m=0}^2 U_m \left[\int_{\hat{y}=-1}^{\hat{y}=1} T_{j+m} T_k \omega d\hat{y} + \int_{\hat{y}=-1}^{\hat{y}=1} T_{|j-m|} T_k \omega d\hat{y} \right] \\ &= \frac{1}{2} \sum_{m=0}^2 U_m [\langle T_{j+m}, T_k \rangle + \langle T_{|j-m|}, T_k \rangle] \end{aligned} \quad (3.36)$$

where the inner products of the individual Chebyshev polynomials are expressed by (3.27). The other inner products involving the reference flow quantities are evaluated in a similar manner.

3.2.2 Discretization of the Boundary Conditions

Substitution of (3.14) into (2.9) provides the modal form of the boundary conditions, i.e.

$$\sum_{n=-N_M}^{N_M} \sum_{m=-M_M}^{M_M} u^{(n,m)}(\hat{y}_U(x, z)) e^{i(n\alpha x + m\beta z)} = -u_0(\hat{y}_U), \quad (3.37a)$$

$$\sum_{n=-N_M}^{N_M} \sum_{m=-M_M}^{M_M} u^{(n,m)}(\hat{y}_L(x, z)) e^{i(n\alpha x + m\beta z)} = -u_0(\hat{y}_L), \quad (3.37b)$$

$$\sum_{n=-N_M}^{N_M} \sum_{m=-M_M}^{M_M} v^{(n,m)}(\hat{y}_U(x, z)) e^{i(n\alpha x + m\beta z)} = 0, \quad (3.37c)$$

$$\sum_{n=-N_M}^{N_M} \sum_{m=-M_M}^{M_M} v^{(n,m)}(\hat{y}_L(x, z)) e^{i(n\alpha x + m\beta z)} = 0, \quad (3.37d)$$

$$\sum_{n=-N_M}^{N_M} \sum_{m=-M_M}^{M_M} w^{(n,m)}(\hat{y}_U(x, z)) e^{i(n\alpha x + m\beta z)} = -w_0(\hat{y}_U), \quad (3.37e)$$

$$\sum_{n=-N_M}^{N_M} \sum_{m=-M_M}^{M_M} w^{(n,m)}(\hat{y}_L(x, z)) e^{i(n\alpha x + m\beta z)} = -w_0(\hat{y}_L). \quad (3.37f)$$

The form of these conditions expressed in terms of v_1 and η_1 is obtained by substituting (3.18) into (3.37), i.e.

$$\begin{aligned} \sum_{\substack{n=-N_M \\ (n,m) \neq (0,0)}}^{N_M} \sum_{m=-M_M}^{M_M} \frac{1}{k_{nm}^2} [in\alpha D v^{(n,m)}(\hat{y}_U(x, z)) - im\beta \eta^{(n,m)}(\hat{y}_U(x, z))] e^{i(n\alpha x + m\beta z)} \\ + u^{(0,0)}(\hat{y}_U(x, z)) = -u_0(\hat{y}_U), \end{aligned} \quad (3.38a)$$

$$\begin{aligned} \sum_{\substack{n=-N_M \\ (n,m) \neq (0,0)}}^{N_M} \sum_{m=-M_M}^{M_M} \frac{1}{k_{nm}^2} [in\alpha D v^{(n,m)}(\hat{y}_L(x, z)) - im\beta \eta^{(n,m)}(\hat{y}_L(x, z))] e^{i(n\alpha x + m\beta z)} \\ + u^{(0,0)}(\hat{y}_L(x, z)) = -u_0(\hat{y}_L), \end{aligned} \quad (3.38b)$$

$$\sum_{n=-N_M}^{N_M} \sum_{m=-M_M}^{M_M} v^{(n,m)}(\hat{y}_U(x, z)) e^{i(n\alpha x + m\beta z)} = 0, \quad (3.38c)$$

$$\sum_{n=-N_M}^{N_M} \sum_{m=-M_M}^{M_M} v^{(n,m)}(\hat{y}_L(x, z)) e^{i(n\alpha x + m\beta z)} = 0, \quad (3.38d)$$

$$\begin{aligned} \sum_{\substack{n=-N_M \\ (n,m) \neq (0,0)}}^{N_M} \sum_{m=-M_M}^{M_M} \frac{1}{k_{nm}^2} [im\beta D v^{(n,m)}(\hat{y}_U(x, z)) + in\alpha \eta^{(n,m)}(\hat{y}_U(x, z))] e^{i(n\alpha x + m\beta z)} \\ + w^{(0,0)}(\hat{y}_U(x, z)) = -w_0(\hat{y}_U), \end{aligned} \quad (3.38e)$$

$$\sum_{\substack{n=-N_M \\ (n,m) \neq (0,0)}}^{N_M} \sum_{m=-M_M}^{M_M} \frac{1}{k_{nm}^2} \left[im\beta Dv^{(n,m)}(\hat{y}_L(x,z)) + in\alpha\eta^{(n,m)}(\hat{y}_L(x,z)) \right] e^{i(n\alpha x + m\beta z)} + w^{(0,0)}(\hat{y}_L(x,z)) = -w_0(\hat{y}_L). \quad (3.38f)$$

The above relations involve all modal functions due to the irregularity of the rough walls; they can be separated into boundary conditions for the individual modal functions in the case of smooth walls.

We shall now discuss the numerical implementation of the above conditions. The discussion is limited to the condition for u_1 at the upper wall as the remaining conditions can be treated in a similar manner.

Substituting (3.20) into (3.38a) we obtain

$$\sum_{\substack{n=-N_M \\ (n,m) \neq (0,0)}}^{N_M} \sum_{m=-M_M}^{M_M} \frac{1}{k_{nm}^2} \left[\sum_{k=0}^{N_T-1} v_k^{(n,m)} DT_k(\hat{y}_U(x,z)) - im\beta \sum_{k=0}^{N_T-1} \eta_k^{(n,m)} T_k(\hat{y}_U(x,z)) \right] e^{i(n\alpha x + m\beta z)} + \sum_{k=0}^{N_T-1} u_k^{(0,0)} T_k(\hat{y}_U(x,z)) = -u_0(\hat{y}_U(x,z)) \quad (3.39)$$

Values of Chebyshev polynomials, their first derivative as well as u_0 and w_0 evaluated at the rough wall represent periodic functions which can be expressed in terms of Fourier expansions of the form

$$T_k(\hat{y}_U(x,z)) = \sum_{n=-((N_T-1) \times N_A)}^{((N_T-1) \times N_A)} \sum_{m=-((N_T-1) \times M_A)}^{((N_T-1) \times M_A)} (CU)_k^{(n,m)} e^{i(n\alpha x + m\beta z)}, \quad (3.40a)$$

$$DT_k(\hat{y}_U(x,z)) = \sum_{n=-((N_T-1) \times N_A)}^{((N_T-1) \times N_A)} \sum_{m=-((N_T-1) \times M_A)}^{((N_T-1) \times M_A)} (EU)_k^{(n,m)} e^{i(n\alpha x + m\beta z)}, \quad (3.40b)$$

$$u_0(\hat{y}_U(x,z)) = \sum_{n=-2N_A}^{2N_A} \sum_{m=-2M_A}^{2M_A} (U_0)^{(n,m)} e^{i(n\alpha x + m\beta z)}, \quad (3.40c)$$

$$w_0(\hat{y}_U(x,z)) = \sum_{n=-2N_A}^{2N_A} \sum_{m=-2M_A}^{2M_A} (W_0^U)^{(n,m)} e^{i(n\alpha x + m\beta z)}. \quad (3.40d)$$

In the above, $(CU)_k^{(n,m)}$, $(EU)_k^{(n,m)}$, $(U_0^U)_k^{(n,m)}$ and $(W_0^U)_k^{(n,m)}$ are the known Fourier expansion coefficients for $T_k(\hat{y}_U)$, $DT_k(\hat{y}_U)$, $u_0(\hat{y}_U)$ and $w_0(\hat{y}_U)$, respectively. The process leading to the evaluation of these coefficients is explained in Appendix C. When the shape of the rough wall is described using N_A Fourier coefficients in the x -direction, the Fourier expansion describing values of the Chebyshev polynomial of order $(N_T - 1)$ evaluated at this wall involves $(N_T - 1) \times N_A$ terms, which explains the summation limit in the x -direction in (3.40). Since velocity components of the reference flow are quadratic functions of \hat{y}_U , their values evaluated at the rough wall involve $2N_A$ Fourier coefficients. Similar arguments explain the limits of expansions in the z -direction.

Substitution of (3.40) into (3.39) and separation of Fourier modes result in

$$\begin{aligned} \sum_{\substack{p=-N_M \\ (p,q) \neq (0,0)}}^{N_M} \sum_{q=-M_M}^{M_M} \sum_{k=0}^{N_T-1} \frac{1}{k_{pq}^2} \left[ip\alpha v_k^{(p,q)} (EU)_k^{(n-p,m-q)} - iq\beta\eta_k^{(p,q)} (CU)_k^{(n-p,m-q)} \right] \\ + \sum_{k=0}^{N_T-1} u_k^{(0,0)} (CU)_k^{(n,m)} = -(U_0^U)^{(n,m)}. \end{aligned} \quad (3.41)$$

In the above, $-N_U \leq n \leq N_U$, $-M_U \leq m \leq M_U$ where $N_U = (N_T - 1) \times N_A + N_M$ and $M_U = (N_T - 1) \times M_A + M_M$. Equation (3.41) provides $(2N_U + 1)(2M_U + 1)$ boundary relations. Their enforcement guarantees the enforcement of the physical boundary condition at the rough wall. As the discretization of the field equations resulted in only $(2N_M + 1)(2M_M + 1)$ equations, one can either retain only the leading $(2N_M + 1)(2M_M + 1)$ of the boundary relations or enforce more boundary relations resulting in the over-determined system.

The final form of all boundary relations can be written as follows

$$\begin{aligned} \sum_{\substack{p=-N_M \\ (p,q) \neq (0,0)}}^{N_M} \sum_{q=-M_M}^{M_M} \sum_{k=0}^{N_T-1} \frac{1}{k_{pq}^2} \left[ip\alpha v_k^{(p,q)} (EU)_k^{(n-p,m-q)} - iq\beta\eta_k^{(p,q)} (CU)_k^{(n-p,m-q)} \right] \\ + \sum_{k=0}^{N_T-1} u_k^{(0,0)} (CU)_k^{(n,m)} = -(U_0^U)^{(n,m)}, \end{aligned} \quad (3.42a)$$

$$\sum_{\substack{p=-N_M \\ (p,q) \neq (0,0)}}^{N_M} \sum_{q=-M_M}^{M_M} \sum_{k=0}^{N_T-1} \frac{1}{k_{pq}^2} \left[ip\alpha v_k^{(p,q)} (EL)_k^{(n-p,m-q)} - iq\beta\eta_k^{(p,q)} (CL)_k^{(n-p,m-q)} \right]$$

$$+ \sum_{k=0}^{N_T-1} u_k^{(0,0)} (CL)_k^{(n,m)} = -(U_0^L)^{(n,m)}, \quad (3.42b)$$

$$\sum_{p=-N_M}^{N_M} \sum_{q=-M_M}^{M_M} \sum_{k=0}^{N_T-1} v_k^{(p,q)} (CU)_k^{(n-p,m-q)} = 0, \quad (3.42c)$$

$$\sum_{p=-N_M}^{N_M} \sum_{q=-M_M}^{M_M} \sum_{k=0}^{N_T-1} v_k^{(p,q)} (CL)_k^{(n-p,m-q)} = 0, \quad (3.42d)$$

$$\begin{aligned} \sum_{\substack{p=-N_M \\ (p,q) \neq (0,0)}}^{N_M} \sum_{q=-M_M}^{M_M} \sum_{k=0}^{N_T-1} \frac{1}{k_{pq}^2} \left[ip\alpha v_k^{(p,q)} (EU)_k^{(n-p,m-q)} - iq\beta \eta_k^{(p,q)} (CU)_k^{(n-p,m-q)} \right] \\ + \sum_{k=0}^{N_T-1} w_k^{(0,0)} (CU)_k^{(n,m)} = -(W_0^U)^{(n,m)}, \end{aligned} \quad (3.42e)$$

$$\begin{aligned} \sum_{\substack{p=-N_M \\ (p,q) \neq (0,0)}}^{N_M} \sum_{q=-M_M}^{M_M} \sum_{k=0}^{N_T-1} \frac{1}{k_{pq}^2} \left[ip\alpha v_k^{(p,q)} (EL)_k^{(n-p,m-q)} - iq\beta \eta_k^{(p,q)} (CL)_k^{(n-p,m-q)} \right] \\ + \sum_{k=0}^{N_T-1} w_k^{(0,0)} (CL)_k^{(n,m)} = -(W_0^L)^{(n,m)}, \end{aligned} \quad (3.42f)$$

where $-N_M \leq n \leq N_M$, $-M_M \leq m \leq M_M$. The reader may note that boundary relations for $(n, m) = (0, 0)$ come naturally from (3.42a)-(3.42b) and (3.42e)-(3.42f).

3.2.3 Discretization of the Flow Rate Constraint

In the case of the fixed pressure gradient constraints, e'_x and e'_z in (3.19) are known and the discretization process is complete. In the case of the fixed flow rate constraints, one needs to discretize these constraints in order to construct conditions required for the determination of e'_x and e'_z . We shall now discuss the discretization of the flow rate constraint in the x -direction as discretization in the z -direction follows the same path.

The flow rate in the x -direction can be expressed as

$$\begin{aligned} Q_x(x) &= \frac{1}{2\pi/\beta} \int_0^{2\pi/\beta} \int_{y_L(x,z)}^{y_U(x,z)} u(x, y, z) dy dz \\ &= \frac{1}{2\pi/\beta} \int_0^{2\pi/\beta} \int_{y_L(x,z)}^{y_U(x,z)} [u_0(y) + u_1(x, y, z)] dy dz \\ &= \frac{1}{2\pi/\beta} \int_0^{2\pi/\beta} \int_{y_L(x,z)}^{y_U(x,z)} u_0(y) dy dz + \frac{1}{2\pi/\beta} \int_0^{2\pi/\beta} \int_{y_L(x,z)}^{y_U(x,z)} u_1(x, y, z) dy dz \end{aligned}$$

$$= \frac{1}{2\pi/\beta} I_{u_0}(x) + \frac{1}{2\pi/\beta} I_{u_1}(x) \quad (3.43)$$

The first integral on the right hand side of (3.43) involves only the reference flow quantities and can be evaluated as follows

$$\begin{aligned} I_{u_0}(x) &= \int_0^{2\pi/\beta} u_0(y) dy dz \\ &= \frac{Re}{2} e_x \int_0^{2\pi/\beta} \int_{y_L(x,z)}^{y_U(x,z)} (1 - y^2) dy dz \\ &= \frac{Re}{2} e_x \int_0^{2\pi/\beta} \left[y_U(x, z) - y_L(x, z) - \frac{y_U^3(x, z) - y_L^3(x, z)}{3} \right] dz \end{aligned} \quad (3.44)$$

where

$$y = a\hat{y} + b, \quad a = \Gamma^{-1}, \quad b = -\Gamma^{-1} + 1 + y_t. \quad (3.45)$$

Substituting (3.45) into (3.44) results in

$$\begin{aligned} I_{u_0}(x) &= \frac{Re}{2} e_x \int_0^{2\pi/\beta} \left[-a^3/3 (\hat{y}_U^3(x, z) - \hat{y}_L^3(x, z)) - a^2 b (\hat{y}_U^2(x, z) - \hat{y}_L^2(x, z)) \right. \\ &\quad \left. - a(b^2 - 1) (\hat{y}_U(x, z) - \hat{y}_L(x, z)) \right] dz \end{aligned} \quad (3.46)$$

to be followed by expressing \hat{y} , \hat{y}^2 and \hat{y}^3 in terms of Chebyshev polynomials, i.e.

$$\hat{y} = T_1(\hat{y}), \quad \hat{y}^2 = (T_2(\hat{y}) + T_0(\hat{y}))/2, \quad \hat{y}^3 = (T_3(\hat{y}) - 3T_1(\hat{y}))/4. \quad (3.47)$$

The resulting expression has the form of

$$\begin{aligned} I_{u_0}(x) &= \frac{Re}{2} e_x \int_0^{2\pi/\beta} \left[\sum_{n=-NS}^{NS} \sum_{m=-MS}^{MS} \left\{ -a^3/12 \left((CU)_3^{(n,m)} - (CL)_3^{(n,m)} \right) - \right. \right. \\ &\quad \left. \left. a^2 b/2 \left((CU)_2^{(n,m)} - (CL)_2^{(n,m)} \right) + (-a^3/4 - a(b^2 - 1)) \left((CU)_1^{(n,m)} - (CL)_1^{(n,m)} \right) - \right. \right. \\ &\quad \left. \left. a^2 b/2 \left((CU)_0^{(n,m)} - (CL)_0^{(n,m)} \right) \right\} e^{inax} e^{im\beta z} \right] dz \end{aligned} \quad (3.48)$$

where advantage has been taken of (3.40a) and $NS = (N_T - 1)N_A$ and $MS = (N_T - 1)M_A$. Since

$$\int_0^{2\pi/\beta} e^{im\beta z} dz = \begin{cases} 0, & m \neq 0 \\ \frac{2\pi}{\beta}, & m = 0 \end{cases}, \quad (3.49)$$

the final expression for $I_{u_0}(x)$ has the following form

$$\begin{aligned}
I_{u_0}(x) &= \frac{Re}{2} e_x \left(\frac{2\pi}{\beta} \right) \sum_{n=-NS}^{NS} \left\{ -a^3/12 \left((CU)_3^{(n,0)} - (CL)_3^{(n,0)} \right) \right. \\
&- a^2 b/2 \left((CU)_2^{(n,0)} - (CL)_2^{(n,0)} \right) + (-a^3/4 - a(b^2 - 1)) \left((CU)_1^{(n,0)} - (CL)_1^{(n,0)} \right) \\
&\left. - a^2 b/2 \left((CU)_0^{(n,0)} - (CL)_0^{(n,0)} \right) \right\} e^{inax}. \quad (3.50)
\end{aligned}$$

The evaluation of the second integral begins by using u_1 in discretized form and expressing its modal functions in terms of the wall-normal velocity and vorticity for all modes except mode (0,0). This process leads to

$$\begin{aligned}
I_{u_1} &= \int_0^{2\pi/\beta} \int_{y_L(x,z)}^{y_U(x,z)} u_1(x, y, z) dy dz = \Gamma^{-1} \int_0^{2\pi/\beta} \int_{\hat{y}_L(x,z)}^{\hat{y}_U(x,z)} u_1(x, \hat{y}, z) d\hat{y} dz \\
&= \Gamma^{-1} \int_0^{2\pi/\beta} \int_{\hat{y}_L(x,z)}^{\hat{y}_U(x,z)} \sum_{k=0}^{N_T-1} u_k^{(0,0)} T_k(\hat{y}) d\hat{y} dz + \\
&\quad \Gamma^{-1} \int_0^{2\pi/\beta} \int_{\hat{y}_L(x,z)}^{\hat{y}_U(x,z)} \sum_{\substack{n=-N_M \\ (n,m) \neq (0,0)}}^{N_M} \sum_{m=-M_M}^{M_M} \sum_{k=0}^{N_T-1} \frac{1}{k_{nm}^2} \left[in\alpha v_k^{(n,m)} DT_k(\hat{y}) - \right. \\
&\quad \left. im\beta \eta_k^{(n,m)} T_k(\hat{y}) \right] e^{i(nax+m\beta z)} d\hat{y} dz \\
&= \Gamma^{-1} \sum_{k=0}^{N_T-1} \left\{ u_k^{(0,0)} \int_0^{2\pi/\beta} I_k(x, z) dz \right\} \\
&+ \Gamma^{-1} \sum_{\substack{n=-N_M \\ (n,m) \neq (0,0)}}^{N_M} \sum_{m=-M_M}^{M_M} \sum_{k=0}^{N_T-1} \left\{ \frac{1}{k_{nm}^2} \left(in\alpha v_k^{(n,m)} e^{inax} \right) \int_0^{2\pi/\beta} J_k(x, z) e^{im\beta z} dz \right\} \\
&- \Gamma^{-1} \sum_{\substack{n=-N_M \\ (n,m) \neq (0,0)}}^{N_M} \sum_{m=-M_M}^{M_M} \sum_{k=0}^{N_T-1} \left\{ \frac{1}{k_{nm}^2} \left(im\beta \eta_k^{(n,m)} e^{inax} \right) \int_0^{2\pi/\beta} I_k(x, z) e^{im\beta z} dz \right\}, \quad (3.51)
\end{aligned}$$

where

$$I_k(x, z) = \left[\int_{\hat{y}_L(x,z)}^{\hat{y}_U(x,z)} T_k(\hat{y}) d\hat{y} \right], \quad (3.52a)$$

$$J_k(x, z) = \left[\int_{\hat{y}_L(x,z)}^{\hat{y}_U(x,z)} DT_k(\hat{y}) d\hat{y} \right] = T_k(\hat{y}_U) - T_k(\hat{y}_L). \quad (3.52b)$$

The analytical evaluation of the integral $I_k(x, z)$ results in

$$I_0(x, z) = T_1(\hat{y}_U) - T_1(\hat{y}_L), \quad I_1(x, z) = \frac{1}{4} (T_2(\hat{y}_U) - T_2(\hat{y}_L)) \quad (3.53a)$$

$$I_k(x, z) = \frac{1}{2} \left[\frac{T_{k+1}(\hat{y}_U) - T_{k+1}(\hat{y}_L)}{k+1} - \frac{T_{k-1}(\hat{y}_U) - T_{k-1}(\hat{y}_L)}{k-1} \right], \quad k > 1. \quad (3.53b)$$

Since the geometry is periodic, functions formed by values of the Chebyshev polynomials evaluated at the upper wall are periodic and, thus, one can write expressions for $I_k(x, z)$ and $J_k(x, z)$, with the help of (3.40a) in the form of

$$I_k(x, z) = \sum_{n=-NS}^{NS} \sum_{m=-MS}^{MS} I_k^{(n,m)} e^{i(nax+m\beta z)}, \quad (3.54a)$$

$$J_k(x, z) = \sum_{n=-NS}^{NS} \sum_{m=-MS}^{MS} J_k^{(n,m)} e^{i(nax+m\beta z)}, \quad (3.54b)$$

where

$$I_0^{(n,m)} = (CU)_1^{(n,m)} - (CL)_1^{(n,m)}, \quad I_1^{(n,m)} = \frac{1}{4} \left((CU)_2^{(n,m)} - (CL)_2^{(n,m)} \right) \quad (3.55a)$$

$$I_k^{(n,m)} = \frac{1}{2} \left[\frac{(CU)_{k+1}^{(n,m)} - (CL)_{k+1}^{(n,m)}}{k+1} - \frac{(CU)_{k-1}^{(n,m)} - (CL)_{k-1}^{(n,m)}}{k-1} \right], \quad k > 1, \quad (3.55b)$$

$$J_k^{(n,m)} = (CU)_k^{(n,m)} - (CL)_k^{(n,m)}. \quad (3.56)$$

Substituting (3.54) into (3.51) results in

$$\begin{aligned} I_{u_1}(x) = & \Gamma^{-1} \sum_{p=-NS}^{NS} \sum_{q=-MS}^{MS} \sum_{k=0}^{N_T-1} \left\{ u_k^{(0,0)} I_k^{(p,q)} e^{ipax} \int_0^{2\pi/\beta} e^{iq\beta z} dz \right\} \\ & + \Gamma^{-1} \sum_{\substack{n=-N_M \\ (n,m) \neq (0,0)}}^{N_M} \sum_{m=-M_M}^{M_M} \sum_{p=-NS}^{NS} \sum_{q=-MS}^{MS} \sum_{k=0}^{N_T-1} \left\{ \frac{1}{k_{nm}^2} i n \alpha v_k^{(n,m)} J_k^{(p,q)} e^{i(n+p)ax} \int_0^{2\pi/\beta} e^{i(q+m)\beta z} dz \right\} \\ & - \Gamma^{-1} \sum_{\substack{n=-N_M \\ (n,m) \neq (0,0)}}^{N_M} \sum_{m=-M_M}^{M_M} \sum_{p=-NS}^{NS} \sum_{q=-MS}^{MS} \sum_{k=0}^{N_T-1} \left\{ \frac{1}{k_{nm}^2} i m \beta \eta_k^{(n,m)} I_k^{(p,q)} e^{i(n+p)ax} \int_0^{2\pi/\beta} e^{i(q+m)\beta z} dz \right\} \end{aligned} \quad (3.57)$$

Since

$$\int_0^{2\pi/\beta} e^{i(q+m)\beta z} dz = \begin{cases} 0, & q \neq -m \\ \frac{2\pi}{\beta}, & q = -m \end{cases}, \quad (3.58)$$

one obtains

$$\begin{aligned}
I_{u_1}(x) &= \frac{2\pi}{\Gamma\beta} \left\{ \sum_{p=-NS}^{NS} \sum_{k=0}^{N_T-1} u_k^{(0,0)} I_k^{(p,0)} e^{ip\alpha x} \right. \\
&+ \left. \sum_{\substack{n=-N_M \\ (n,m) \neq (0,0)}}^{N_M} \sum_{m=-M_M}^{M_M} \sum_{p=-NS}^{NS} \sum_{k=0}^{N_T-1} \frac{i n \alpha v_k^{(n,m)} J_k^{(p,-m)} - i m \beta \eta_k^{(n,m)} I_k^{(p,-m)}}{k_{nm}^2} e^{i(n+p)\alpha x} \right\}, \quad (3.59)
\end{aligned}$$

Re-naming the indices results in

$$\begin{aligned}
I_{u_1}(x) &= \frac{2\pi}{\Gamma\beta} \left\{ \sum_{n=-NS}^{NS} \sum_{k=0}^{N_T-1} u_k^{(0,0)} I_k^{(n,0)} e^{in\alpha x} \right. \\
&+ \left. \sum_{\substack{p=-N_M \\ (p,m) \neq (0,0)}}^{N_M} \sum_{m=-M_M}^{M_M} \sum_{n=-NQ}^{NQ} \sum_{k=0}^{N_T-1} \frac{i p \alpha v_k^{(p,m)} J_k^{(n-p,-m)} - i m \beta \eta_k^{(p,m)} I_k^{(n-p,-m)}}{k_{pm}^2} e^{in\alpha x} \right\} \quad (3.60)
\end{aligned}$$

where $NQ = NS + N_M$.

Substituting the expressions for $I_{u_0}(x)$ and $I_{u_1}(x)$ into (3.43) and replacing the index m with q results in the discretized expression for the flow rate of the form

$$\begin{aligned}
Q_x(x) &= \frac{Re}{2} e_x \left(\frac{2\pi}{\beta} \right) \sum_{n=-NS}^{NS} \left\{ -a^3/12 \left((CU)_3^{(n,0)} - (CL)_3^{(n,0)} \right) \right. \\
&- a^2 b/2 \left((CU)_2^{(n,0)} - (CL)_2^{(n,0)} \right) + (-a^3/4 - a(b^2 - 1)) \left((CU)_1^{(n,0)} - (CL)_1^{(n,0)} \right) \\
&- \left. a^2 b/2 \left((CU)_0^{(n,0)} - (CL)_0^{(n,0)} \right) \right\} e^{in\alpha x} \\
&+ \frac{2\pi}{\Gamma\beta} \left\{ \sum_{n=-NS}^{NS} \sum_{k=0}^{N_T-1} u_k^{(0,0)} I_k^{(n,0)} e^{in\alpha x} \right. \\
&+ \left. \sum_{\substack{p=-N_M \\ (p,q) \neq (0,0)}}^{N_M} \sum_{q=-M_M}^{M_M} \sum_{n=-NQ}^{NQ} \sum_{k=0}^{N_T-1} \frac{i p \alpha v_k^{(p,q)} J_k^{(n-p,-q)} - i q \beta \eta_k^{(p,q)} I_k^{(n-p,-q)}}{k_{pq}^2} e^{in\alpha x} \right\} \quad (3.61)
\end{aligned}$$

which demonstrates that the flow rate is a periodic function of x . This expression can be written in a simpler form of

$$Q_x(x) = \sum_{n=-\infty}^{\infty} Q_x^{(n)} e^{in\alpha x}. \quad (3.62)$$

In the case of the fixed volume flow rate constraint, mode zero of the above expression represents the mean flow and has to be specified. The mean flow rate has two components, i.e.

$$Q_x^{(0)} = Q_{x0} + Q_{x1} \quad (3.63)$$

where Q_{x0} stands for the flow rate of the reference flow and Q_{x1} represents the flow rate modification due to the presence of the roughness. Extracting mode zero from (3.61) results in

$$\begin{aligned} Q_x^{(0)} = & \frac{Re}{2} e_x \left(\frac{2\pi}{\beta} \right) \left\{ -a^3/12 \left((CU)_3^{(0,0)} - (CL)_3^{(0,0)} \right) \right. \\ & - a^2 b/2 \left((CU)_2^{(0,0)} - (CL)_2^{(0,0)} \right) + (-a^3/4 - a(b^2 - 1)) \left((CU)_1^{(0,0)} - (CL)_1^{(0,0)} \right) \\ & \left. - a^2 b/2 \left((CU)_0^{(0,0)} - (CL)_0^{(0,0)} \right) \right\} + \\ & \frac{2\pi}{\Gamma\beta} \left\{ \sum_{k=0}^{N_T-1} u_k^{(0,0)} I_k^{(0,0)} + \sum_{\substack{p=-N_M \\ (p,q) \neq (0,0)}}^{N_M} \sum_{q=-N_M}^{N_M} \sum_{k=0}^{N_T-1} \frac{ip\alpha v_k^{(p,q)} J_k^{(-p,-q)} - iq\beta\eta_k^{(p,q)} I_k^{(-p,-q)}}{k_{pq}^2} \right\} \quad (3.64) \end{aligned}$$

Substitution of (3.64) into (3.63) results in the following form of the flow rate constraint

$$\begin{aligned} & \frac{1}{\Gamma} \sum_{\substack{p=-N_M \\ (p,q) \neq (0,0)}}^{N_M} \sum_{q=-M_M}^{M_M} \sum_{k=0}^{N_T-1} \frac{ip\alpha v_k^{(p,q)} J_k^{(-p,-q)} - iq\beta\eta_k^{(p,q)} I_k^{(-p,-q)}}{k_{pq}^2} + \frac{1}{\Gamma} \sum_{k=0}^{N_T-1} u_k^{(0,0)} I_k^{(0,0)} + \\ & \frac{Re}{2} e_x \left\{ -a^3/12 \left((CU)_3^{(0,0)} - (CL)_3^{(0,0)} \right) \right. \\ & - a^2 b/2 \left((CU)_2^{(0,0)} - (CL)_2^{(0,0)} \right) + (-a^3/4 - a(b^2 - 1)) \left((CU)_1^{(0,0)} - (CL)_1^{(0,0)} \right) \\ & \left. - a^2 b/2 \left((CU)_0^{(0,0)} - (CL)_0^{(0,0)} \right) \right\} = Q_{x0} + Q_{x1} \quad (3.65) \end{aligned}$$

where all unknowns are on the left hand side. A similar procedure applied to the fixed flow rate constraint in the z -direction results in

$$\begin{aligned} & \frac{1}{\Gamma} \sum_{\substack{p=-N_M \\ (p,q) \neq (0,0)}}^{N_M} \sum_{q=-M_M}^{M_M} \sum_{k=0}^{N_T-1} \frac{iq\beta v_k^{(p,q)} J_k^{(-p,-q)} + ip\alpha\eta_k^{(p,q)} I_k^{(-p,-q)}}{k_{pq}^2} + \frac{1}{\Gamma} \sum_{k=0}^{N_T-1} w_k^{(0,0)} I_k^{(0,0)} + \\ & \frac{Re}{2} e_z \left\{ -a^3/12 \left((CU)_3^{(0,0)} - (CL)_3^{(0,0)} \right) \right. \end{aligned}$$

$$\begin{aligned}
& -a^2b/2\left((CU)_2^{(0,0)} - (CL)_2^{(0,0)}\right) + (-a^3/4 - a(b^2 - 1))\left((CU)_1^{(0,0)} - (CL)_1^{(0,0)}\right) \\
& - a^2b/2\left((CU)_0^{(0,0)} - (CL)_0^{(0,0)}\right)\} = Q_{z_0} + Q_{z_1} \tag{3.66}
\end{aligned}$$

Section 4

4 Solution Process

The system (3.25) - (3.26) together with the boundary relations (3.42) and the flow rate constraints (3.65) - (3.66) represents a coupled nonlinear system of algebraic equations. This system is solved using the first-order fixed-point iterative method whose details are described later in this Section. The solution results in the determination of the Chebyshev expansion coefficients of the wall normal velocity, the wall normal vorticity, modes (0, 0) for u_1 and w_1 as well as the pressure gradient corrections in the case of the fixed flow rate constraints. The remaining modal functions for u_1 and w_1 are evaluated using (3.19).

Considering that all the nonlinear terms are placed at the right hand side and are treated as known, one needs to solve a linear system at each iteration step and, subsequently, determine the new approximation for the nonlinear terms. The process of constructing the new approximation for the unknowns can be summarized as follows

$$\{\mathbf{X}\}^{j+1} = \{\mathbf{X}\}^j + RF[\{\mathbf{X}\}^{(comp)} - \{\mathbf{X}\}^j] \quad (4.1)$$

where \mathbf{X} is the vector of unknowns, the superscripts j and $j+1$ identify the current and next approximations, and the superscript *comp* denotes the solution computed at the new iteration. The iteration process is controlled using the under-relaxation parameter RF .

At each iteration step, the nonlinear terms are computed using the information available from the previous iteration. These terms involve velocity products (i.e. $u_1 u_1$, $u_1 v_1$, ...) which are evaluated in the physical space on a grid involving Chebyshev points in the \hat{y} -direction and a uniformly distributed grid in the x - and z -directions. The modal functions for these velocity products (i.e. $\langle u_1 u_1 \rangle^{(n,m)}$, $\langle u_1 v_1 \rangle^{(n,m)}$, ...) are computed using two-dimensional Fast Fourier Transform (FFT) for each Chebyshev point using the 3/2 rule to control the aliasing error [43]. This data is subsequently used to determine the

Chebyshev expansion coefficients of the modal functions using the method described in Appendix B.

The iteration process is continued until a suitable convergence criterion is satisfied. The convergence criterion used in the present work is of the form

$$|[\mathbf{X}]^{(k+1)} - [\mathbf{X}]^{(k)}| / |[\mathbf{X}]^{(k+1)}| < CONV \quad (4.2)$$

where $|[\mathbf{X}]^{(k+1)} - [\mathbf{X}]^{(k)}|$ is the L^2 norm of the difference between the solution vectors computed at two consecutive iterations and $|[\mathbf{X}]^{(k+1)}|$ is the L^2 norm of the current solution vector. $CONV = 10^{-14}$ has been used in all tests reported in this paper. Relaxation factors $RF < 0.1$ were typically used in the computations.

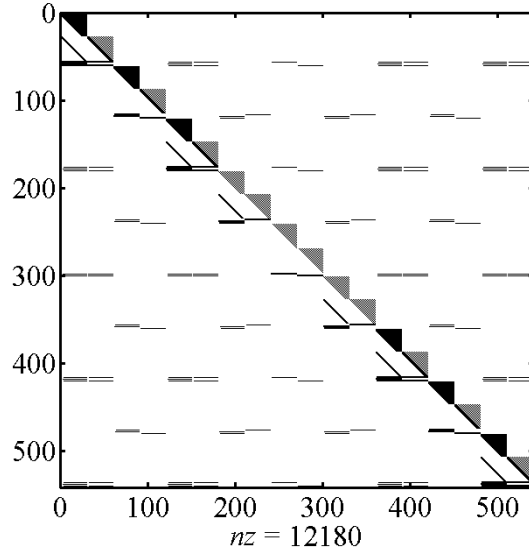
4.1 Specialized Direct Solver

The linear system of equation, which needs to be solved at each iteration step, has the form of

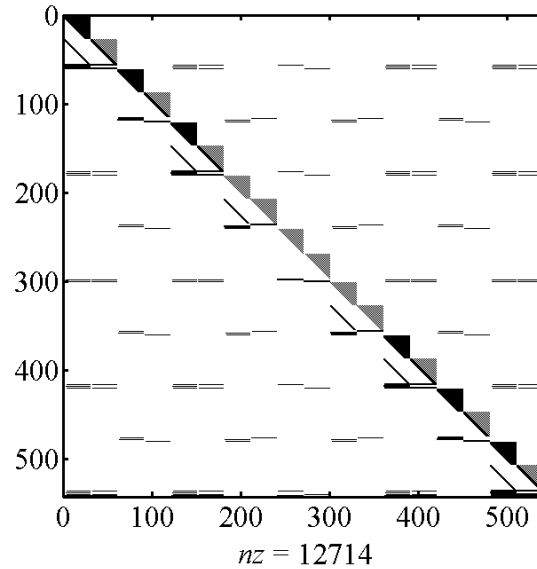
$$\mathbf{LX} = \mathbf{R} \quad (4.3)$$

where \mathbf{L} is the coefficient matrix of the size $p \times p$, with $p = (2N_M + 1)(2M_M + 1)2N_T$ for the fixed pressure gradient case and $p = (2N_M + 1)(2M_M + 1)2N_T + 2$ for the fixed flow rate case. \mathbf{X} is the vector of unknowns with dimension p and \mathbf{R} is the p -dimensional right hand side vector that contains the nonlinear terms. Figure 2 illustrates the structure of \mathbf{L} for both the fixed pressure gradient constraint and the fixed flow rate constraint. The matrix is organized by varying the index for the x -direction from $-N_M$ to N_M and for each such index varying the index for the z -direction from $-M_M$ to M_M . Two blocks are entered for each index pair, one for the velocity and one for the vorticity. As a result, two top left blocks in Fig. 2 represent mode $(-N_M, -M_M)$, two central blocks represent mode $(0,0)$ and the two bottom right blocks represent mode (N_M, M_M) . The computational cost of solving this linear system is potentially very high due to its size. To reduce the cost, a

specialized direct solver which takes advantage of the structure of the coefficient matrix has been developed, following ideas described in [39].



(A)



(B)

Figure 2: Structure of the coefficient matrix L for $N_T = 30$, $N_M = M_M = 1$. For the fixed pressure gradient constraint (Fig. 2A) $p = (2N_M + 1)(2M_M + 1)2N_T$ and for the fixed flow rate constraint (Fig. 2B) $p = (2N_M + 1)(2M_M + 1)2N_T + 2$. The black color identifies the non-zero elements with nz giving their total number. The blocks assume various shades of grey depending on the density of the non-zero elements.

The construction of the efficient solver is described in the context of the fixed pressure gradient constraint. The first step of the solution involves the re-arrangement of the coefficient matrix in such a way that entries corresponding to the field equations are grouped at the upper portion of the matrix while the boundary relations are grouped at the bottom. The second step involves extraction of the largest possible block diagonal matrix from the part of the matrix associated with the field equations. In order to do so, the first four unknowns from each modal velocity equation and the first two unknowns from each modal vorticity equation are moved to the end of the vector of unknowns. For modes $(0, 0)$, the first two unknowns for $u^{(0,0)}$ and $w^{(0,0)}$ are moved to the end of the vector of unknowns. The resultant matrix has the structure illustrated in Fig. 3. Here \mathbf{A} is the largest possible block diagonal structure with invertible blocks. Equation (4.3) can now be written in the form of

$$\mathbf{A}\mathbf{X}_1 + \mathbf{B}\mathbf{X}_2 = \mathbf{R}_1, \quad (4.4a)$$

$$\mathbf{C}\mathbf{X}_1 + \mathbf{D}\mathbf{X}_2 = \mathbf{R}_2. \quad (4.4b)$$

In the above, \mathbf{X}_1 denotes the vector of unknowns of length $S(2N_T - 6) + 2$ that contains all unknown expansion coefficients of the order higher than three for the velocity and higher than one for the vorticity for all Fourier modes except mode $(0,0)$, and contains all unknown expansion coefficients of order higher than one for $u^{(0,0)}$ and $w^{(0,0)}$ where $S = (2N_M + 1)(2M_M + 1)$. \mathbf{X}_2 denotes a vector of length $6S - 2$ that contains the remaining unknowns. Matrices \mathbf{A} , \mathbf{B} , \mathbf{C} and \mathbf{D} have sizes $[S(2N_T - 6) + 2] \times [S(2N_T - 6) + 2]$, $[S(2N_T - 6) + 2] \times [6S - 2]$, $[6S - 2] \times [S(2N_T - 6) + 2]$ and $[6S - 2] \times [6S - 2]$, respectively, while the right hand vectors \mathbf{R}_1 and \mathbf{R}_2 have lengths $S(2N_T - 6) + 2$ and $6S - 2$, respectively.

System (4.4) has a solution of the form

$$\mathbf{X}_2 = (\mathbf{D} - \mathbf{C}\mathbf{A}^{-1}\mathbf{B})^{-1}(\mathbf{R}_2 - \mathbf{C}\mathbf{A}^{-1}\mathbf{R}_1), \quad (4.5a)$$

$$\mathbf{X}_1 = \mathbf{A}^{-1}(\mathbf{R}_1 - \mathbf{B}\mathbf{X}_2). \quad (4.5b)$$

Matrix A consists of the uncoupled blocks associated with each Fourier mode and, thus, can be inverted block by block. This results in a significant reduction of the computational cost.

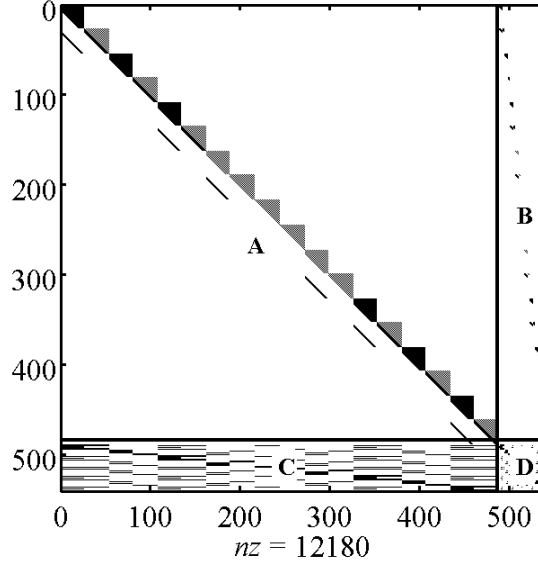


Figure 3: The structure of the re-arranged coefficient matrix for $N_T = 30$, $N_M = M_M = 1$. The black color identifies the non-zero elements with nz giving their total number. The blocks assume various shades of grey depending on the density of the non-zero elements.

Equation (4.5) demonstrates the potential for the development of various solution strategies depending on the aspect of the computational cost which is dominant. In the most memory efficient strategy, each individual set of blocks A_j , B_j , C_j is constructed only when required and deleted immediately after its use. This allows the construction of A^{-1} , CA^{-1} , $CA^{-1}B$, $A^{-1}R_1$ and $A^{-1}B$ block by block rather than working with the complete matrices. Although this method reduces the memory requirement substantially, it is relatively slow in terms of execution time. This happens for two reasons: (i) this strategy requires evaluation of all A_j 's and B_j 's twice, i.e. for evaluation of X_2 and then for evaluation of X_1 , and (ii) R_1 needs to be updated in each iteration which requires re-computation of A_j , B_j and C_j at every iteration. To overcome this difficulty, we compute and save $(D - CA^{-1}B)$, CA^{-1} and $A^{-1}B$ before initiation of the iteration process.

4.2 Implementation of the Reality Conditions

The unknowns are represented in terms of Fourier expansions of the form

$$A(x, y, z) = \sum_{n=-N_M}^{N_M} \sum_{m=-M_M}^{M_M} A^{(n,m)}(y) e^{i(n\alpha x + m\beta z)}. \quad (4.6)$$

The coefficients of these expansions are related through the reality conditions with $A^{(n,m)} = A^{(-n,-m)*}$, $A^{(n,-m)} = A^{(-n,m)*}$ and star denoting the complex conjugate. It is sufficient to solve only for the modal function with the positive n and m indices and the positive n and negative m indices. The first step in the implementation of this property involves separation of the unknowns into the real and imaginary parts, i.e.

$$\eta^{(n,m)} = \eta_r^{(n,m)} + i\eta_i^{(n,m)}, \quad (4.7a)$$

$$u^{(n,m)} = u_r^{(n,m)} + iu_i^{(n,m)}, \quad (4.7b)$$

$$v^{(n,m)} = v_r^{(n,m)} + iv_i^{(n,m)}, \quad (4.7c)$$

$$w^{(n,m)} = w_r^{(n,m)} + iw_i^{(n,m)} \quad (4.7d)$$

where the subscripts r and i denote the real and imaginary parts, respectively. In the second step, the governing equations, the boundary relations and the flow constraints are separated into the real and imaginary parts. This results in a system of two real 4th order and two real 2nd order equations along with 12 boundary conditions for each mode except mode (0,0) and four real 2nd order equations and eight real boundary relations for mode (0,0) for fixed pressure gradient constraint. In case of the fixed flow rate constraint, the real and imaginary parts of the flow constraint equations are added to the system. The Fourier mode indices vary from $(0, -M_M)$ to (N_M, M_M) . A schematic diagram of the coefficient matrix for the fixed pressure gradient constraint is displayed in Fig. 4. The size of the matrix is $s \times s$, where $s = [((N_M + 1)(2M_M + 1))4N_T - 2N_T]$.

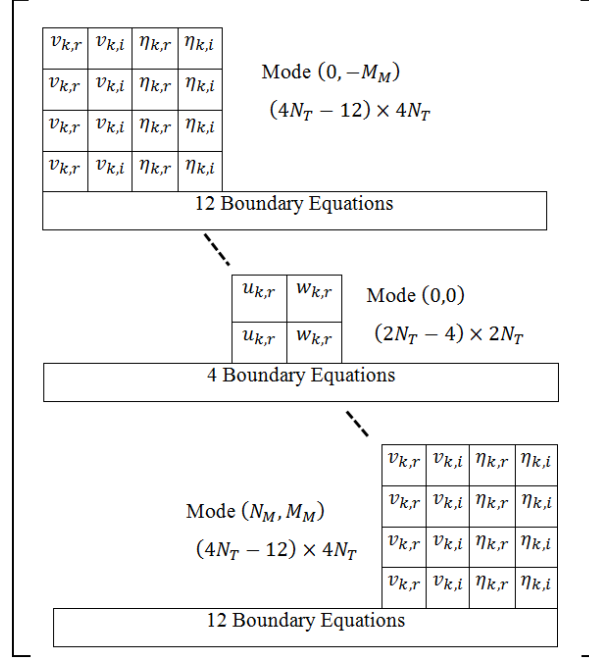
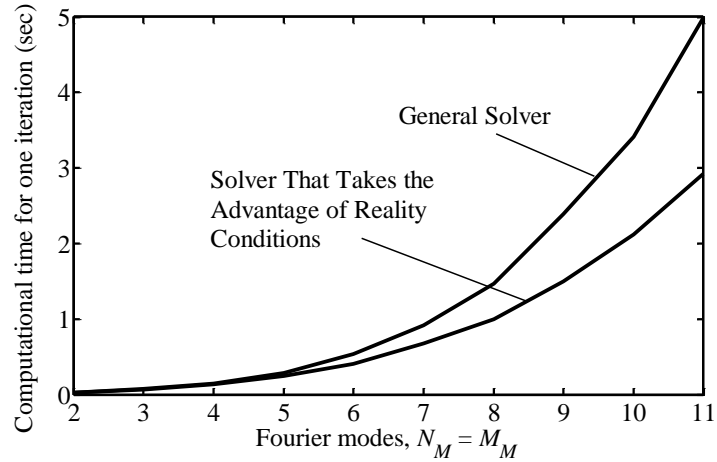
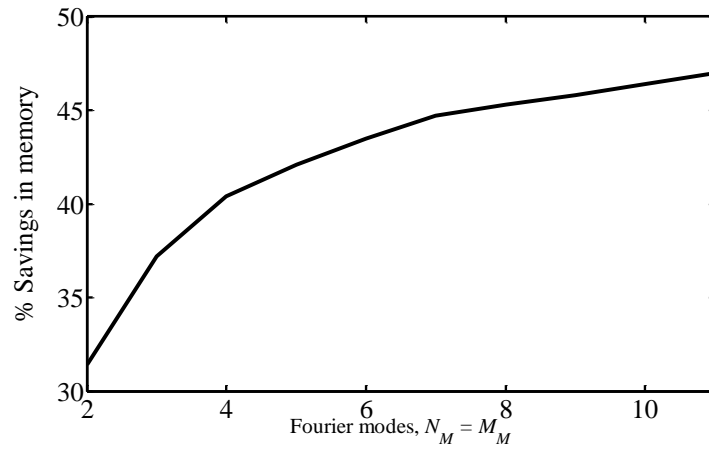


Figure 4: Schematic diagram of the coefficient matrix for the fixed pressure gradient constraint with all unknowns separated into real and imaginary parts. Each small block contains coefficients of the unknowns written in the block.

The system is solved for the real and imaginary parts of the wall-normal velocity and vorticity for all modes except mode $(0,0)$ and for the real parts of $u^{(0,0)}$ and $w^{(0,0)}$. Since the $(0,0)$ mode of v_1 is zero, Eq.(3.18) demonstrates that the imaginary parts of $u^{(0,0)}$ and $w^{(0,0)}$ are also zero. This procedure results in a reduction of the computational time by as much as 40% (Fig. 5A) and reduction of the memory requirement by up to 47% (Fig. 5B) with the advantage increasing with the increase of the number of Fourier modes used.



(A)



(B)

Figure 5: Variations of the computational time per iteration (Fig. 5A) with and without taking advantage of the complex conjugate property and variations of the memory savings when taking advantage of the complex conjugate property (Fig. 5B) as functions of the number of Fourier modes used in the solution. $N_T = 50$ Chebyshev polynomials have been used in the tests.

Section 5

5 Evaluation of the Pressure Field

Evaluation of the pressure field is a part of the post-processing which comes after the determination of the vorticity and velocity fields. We start with the x , y and z -components of the momentum equations (2.3b) of the form

$$u_0 \frac{\partial u_1}{\partial x} + v_0 \frac{\partial u_0}{\partial y} + w_0 \frac{\partial u_1}{\partial z} + \left(u_1 \frac{\partial u_1}{\partial x} + v_1 \frac{\partial u_1}{\partial y} + w_1 \frac{\partial u_1}{\partial z} \right) = -\frac{\partial p_1}{\partial x} + \frac{1}{Re} \left(\frac{\partial^2 u_1}{\partial x^2} + \frac{\partial^2 u_1}{\partial y^2} + \frac{\partial^2 u_1}{\partial z^2} \right), \quad (5.1a)$$

$$u_0 \frac{\partial v_1}{\partial x} + w_0 \frac{\partial v_1}{\partial z} + \left(u_1 \frac{\partial v_1}{\partial x} + v_1 \frac{\partial v_1}{\partial y} + w_1 \frac{\partial v_1}{\partial z} \right) = -\frac{\partial p_1}{\partial y} + \frac{1}{Re} \left(\frac{\partial^2 v_1}{\partial x^2} + \frac{\partial^2 v_1}{\partial y^2} + \frac{\partial^2 v_1}{\partial z^2} \right), \quad (5.1b)$$

$$u_0 \frac{\partial w_1}{\partial x} + v_1 \frac{\partial w_0}{\partial y} + w_0 \frac{\partial w_1}{\partial z} + \left(u_1 \frac{\partial w_1}{\partial x} + v_1 \frac{\partial w_1}{\partial y} + w_1 \frac{\partial w_1}{\partial z} \right) = -\frac{\partial p_1}{\partial z} + \frac{1}{Re} \left(\frac{\partial^2 w_1}{\partial x^2} + \frac{\partial^2 w_1}{\partial y^2} + \frac{\partial^2 w_1}{\partial z^2} \right). \quad (5.1c)$$

Now using the Fourier expansions of the velocity components (3.14b-3.14d) and the expression for pressure (2.7b) we can write the modal function for the pressure as follows

$$p^{(n,m)}(\hat{y}) = -\frac{1}{in\alpha} \left[-\frac{1}{Re} (D^2 - k_{nm}^2) u^{(n,m)}(\hat{y}) + u_0 in\alpha u^{(n,m)}(\hat{y}) + D u_0 v^{(n,m)}(\hat{y}) + w_0 im\beta u^{(n,m)}(\hat{y}) + in\alpha (u_1 u_1)^{(n,m)}(\hat{y}) + im\beta (u_1 w_1)^{(n,m)}(\hat{y}) \right], \text{ for } n \neq 0, \quad (5.2a)$$

$$p^{(0,m)}(\hat{y}) = -\frac{1}{im\beta} \left[-1/Re (D^2 - m^2 \beta^2) w^{(0,m)}(\hat{y}) D w_0 v^{(0,m)}(\hat{y}) + w_0 im\beta w^{(0,m)}(\hat{y}) + D (v_1 w_1)^{(0,m)}(\hat{y}) + im\beta (w_1 w_1)^{(0,m)}(\hat{y}) \right], \text{ for } m = 0, \quad (5.2b)$$

$$p^{(0,0)}(\hat{y}) = -(v_1 v_1)^{(0,0)}(\hat{y}) + c_1, \quad (5.2c)$$

where c_1 is an arbitrary constant.

Substituting the Chebyshev expansions for the velocity components (3.20b)-(3.20d) and velocity products (3.22) and the following for the pressure

$$p^{(n,m)}(\hat{y}) = \sum_{k=0}^{\infty} p_k^{(n,m)} T_k(\hat{y}), \quad (5.3)$$

and using the orthogonality property of the Chebyshev polynomials we get

$$\begin{aligned} p_j^{(n,m)} = & -\frac{2}{ic_j\pi n\alpha} \sum_{k=0}^{N_T-1} \left\{ -\frac{1}{Re} u_k^{(n,m)} \langle T_j, D^2 T_k \rangle \right. \\ & + \left(\frac{k_{im}^2}{Re} u_k^{(n,m)} + in\alpha (G_{uu})_k^{(n,m)} + im\beta (G_{uw})_k^{(n,m)} \right) \langle T_j, T_k \rangle \\ & + (G_{uv})_k^{(n,m)} \langle T_j, DT_k \rangle + in\alpha u_k^{(n,m)} \langle T_j, u_0 T_k \rangle \} \\ & + im\beta u_k^{(n,m)} \langle T_j, w_0 T_k \rangle + v_k^{(n,m)} \langle T_j, Dw_0 T_k \rangle, \quad \text{for } n \neq 0, \end{aligned} \quad (5.4a)$$

$$\begin{aligned} p_j^{(0,m)} = & -\frac{2}{ic_j\pi m\beta} \sum_{k=0}^{N_T-1} \left\{ -\frac{1}{Re} w_k^{(0,m)} \langle T_j, D^2 T_k \rangle \right. \\ & + \left(\frac{m^2\beta^2}{Re} w_k^{(0,m)} + im\beta (G_{ww})_k^{(0,m)} \right) \langle T_j, T_k \rangle \\ & + (G_{vw})_k^{(0,m)} \langle T_j, DT_k \rangle + im\beta w_k^{(0,m)} \langle T_j, w_0 T_k \rangle + v_k^{(0,m)} \langle T_j, Dw_0 T_k \rangle \}, \quad \text{for } m = 0, \end{aligned} \quad (5.4b)$$

$$p_j^{(0,0)} = \frac{2}{c_j\pi} \sum_{k=0}^{N_T-1} - (G_{vv})_k^{(0,0)} \langle T_j, T_k \rangle + c_1, \quad (5.4c)$$

$$\text{where } c_j = \begin{cases} 1 & j \neq 0 \\ 2 & j = 0 \end{cases}.$$

Section 6

6 Performance of the Algorithm

To demonstrate the accuracy of the algorithm, we select a simple model problem with the smooth upper wall and a rough lower wall with the roughness geometry described by one Fourier mode, e.g.

$$y_U = 1, \quad y_L = -1 + y_b \sin(\alpha x) \cos(\beta z). \quad (6.1)$$

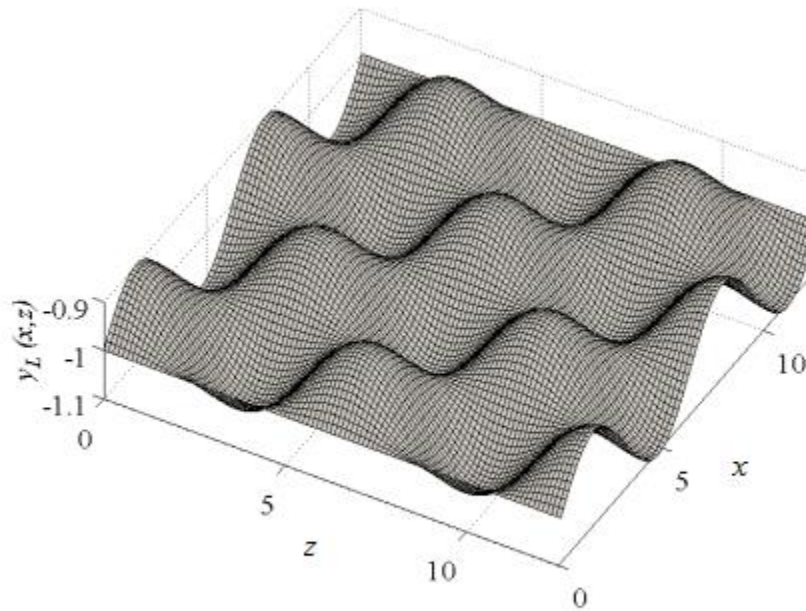


Figure 6: Geometry of the lower wall described by (6.1) with $y_b = 0.1$, $\alpha = \beta = 1$ for two periods in the x - and z -directions.

As the first test, we reproduced results presented in [14] for the transverse grooves ($\beta = 0$). Figure 7 depicts the difference between the velocity fields obtained by the two solvers at narrowest and widest channel opening.

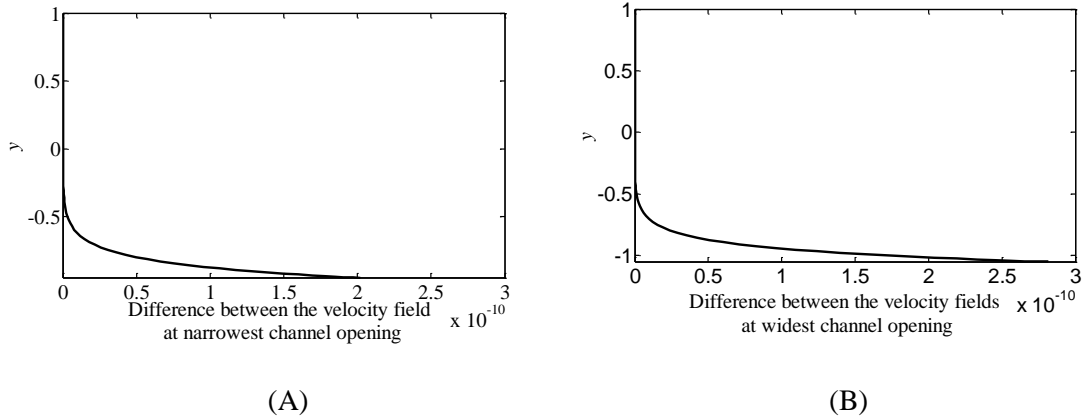


Figure 7: Difference between the velocity fields obtained by current algorithm and algorithm described by [14] for transverse grooves at narrowest channel opening (Fig.7A) and widest channel opening (Fig.7B). Calculations have been carried out with $y_b = 0.05$ and $\alpha = 1$ for $Re = 5$.

As the second test, we reproduced results for the longitudinal grooves ($\alpha = 0$) presented in [14, 15, 35]. Figure 8 presents the difference between the velocity fields between the two solvers at the narrowest and widest channel opening.

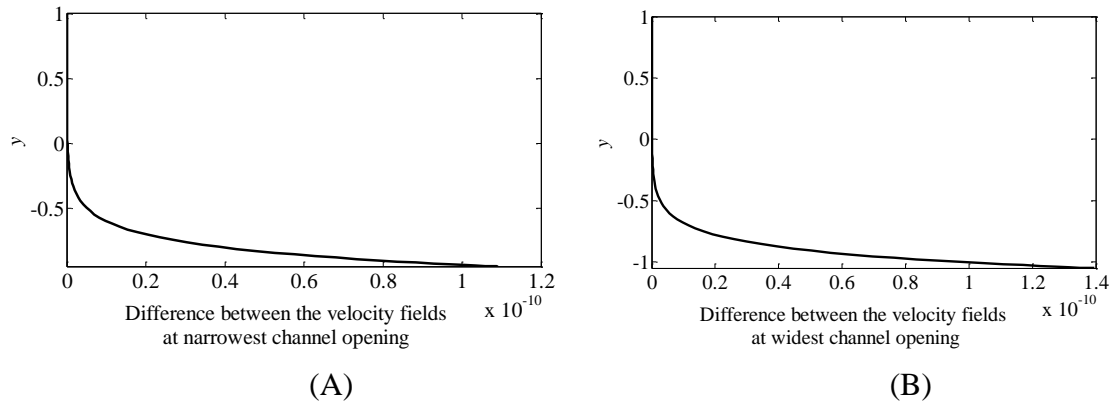


Figure 8: Difference between the velocity fields obtained by current algorithm and algorithm described by [14, 15, 35] for transverse grooves at narrowest channel opening (Fig.8A) and widest channel opening (Fig.8B). Calculations have been carried out with $y_b = 0.05$ and $\beta = 1$ for $Re = 5$.

As the third test, we reproduced results for the straight, two-dimensional grooves inclined with respect to the flow direction presented in [14]. This test is particularly useful as flow over such grooves can be determined using two-dimensional solution coupled with special transformations [14] while in the present case we treat the groove geometry as three-dimensional in the reference system where one axis is aligned with the flow direction and solve it as a three-dimensional problem. In all cases the solution produced using the algorithm presented in this paper agreed within at least 12 digits with the solutions obtained using other methods.

In the rest of this discussion we focus on the demonstration of the spectral accuracy of the three-dimensional algorithm implemented with the fixed pressure gradient constraints with the reference flow directed along the x -axis unless otherwise noted.

Two measures of the solution error have been used. The first measure uses the maximum difference between the computed solution and a reference solution over the whole physical domain. The solution obtained using $N_T = 40$ Chebyshev polynomials and $N_M = M_M = 10$ Fourier modes has been used as the reference solution. The second measure uses the difference between the computed solution at the boundary and the known boundary condition. These measures are defined for the u -velocity component as

$$\|u_{er}\|_{\infty} = \sup|u_{er}(x, y, z)|, \quad 0 \leq x \leq \frac{2\pi}{\alpha}, \quad -1 + y_b \leq y \leq 1 \text{ and } 0 \leq z \leq \frac{2\pi}{\beta}, \quad (6.2a)$$

$$\|u_{er,BC}\|_{\infty} = \sup|u_{er,BC}|, \quad 0 \leq x \leq \frac{2\pi}{\alpha}, \quad 0 \leq z \leq \frac{2\pi}{\beta}, \quad (6.2b)$$

where

$$u_{er}(x, y, z) = u_{computed}(x, y, z) - u_{reference}(x, y, z), \quad (6.3a)$$

$$u_{er,BC}(x, z) = u_{computed}(x, y_L(x, z), z). \quad (6.3b)$$

In a spectrally accurate algorithm the solution should converge exponentially with the increasing number of Chebyshev polynomials. Figure 7 verifies that the algorithm delivers spectral accuracy in the y -direction. While conducting this test, it has been verified that the number of Fourier modes used was sufficient to reduce the associated

error to a low enough level so that the remaining error was dominated by the truncation of Chebyshev expansions.

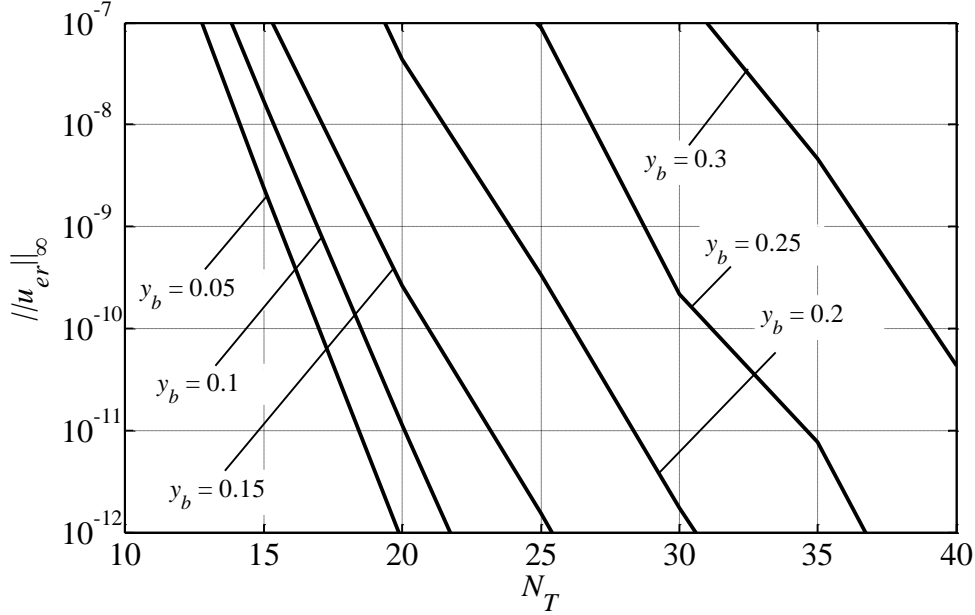
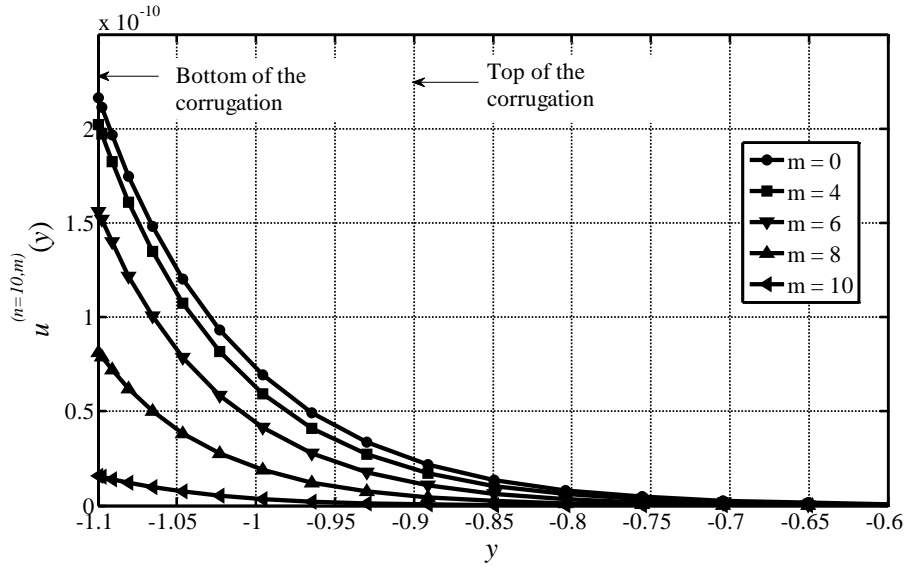
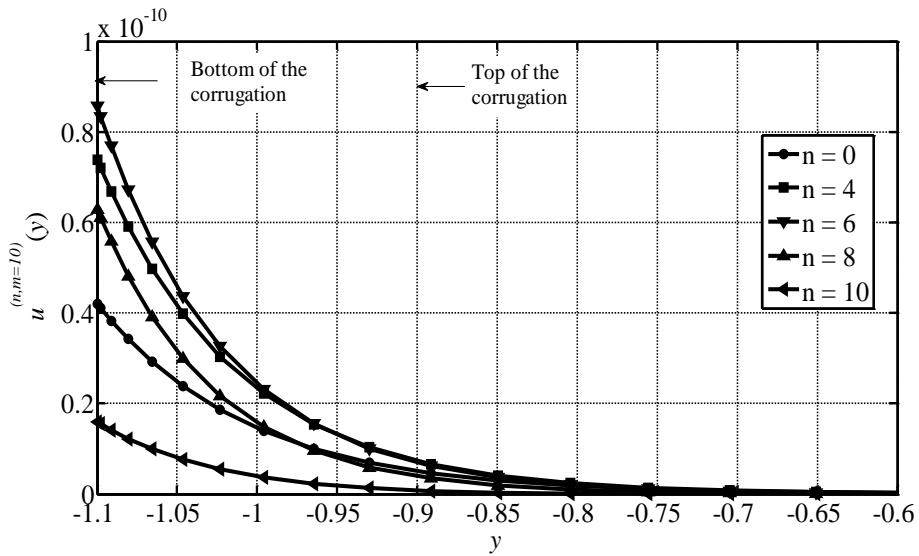


Figure 9: Variation of $\|u_{er}\|_{\infty}$ as a function of the number of Chebyshev polynomials N_T used in the solution. Calculations have been carried out with $N_M = M_M = 10$ for the roughness geometry described by (6.1) with $\alpha = \beta = 1$ for $Re = 5$.

Figure 8 demonstrates that the modal functions develop a boundary layer near the rough boundary. These layers become extremely thin for larger values of the roughness wave number and for higher Fourier modes. The modal functions have rapid variation with respect to y inside the boundary layer, while their value remains close to zero in the rest of the domain. In order to capture these variations and to avoid any spurious oscillation in the distributions of the modal functions, a sufficient number of Chebyshev polynomials should be employed. This implies that in order to reach a certain absolute level of accuracy the number of Chebyshev polynomials needs to be increased with increasing the magnitudes of wave numbers α and/or β (short wavelength roughness), especially when the higher Fourier modes begin to play a significant role in the solution.



(A)



(B)

Figure 10: Variation of the modal functions close to the rough boundary. Calculations have been carried out with $N_T = 40$ for the roughness geometry described by (5.1) $\alpha = \beta = 1$, $y_b = 0.1$ for $Re = 5$. In Fig. 8A, m changes while $n = 10$ and in Fig.8B n changes while $m = 10$. Formation of boundary layers near the rough wall and rapid growth of modal functions across these layers are clearly visible.

The magnitude of the modal functions $v^{(n,m)}$ can be measured using the Chebyshev norm defined as

$$\|v^{(n,m)}\|_{\infty} = \sqrt{\int_{-1}^1 v^{(n,m)} v^{(n,m)*} \omega(\hat{y}) d\hat{y}} . \quad (6.4)$$

Results displayed in Fig. 9 demonstrate that the magnitude of the modal functions decreases exponentially with increasing the mode index, which confirms the spectral convergence of discretization in the x - and z -directions.

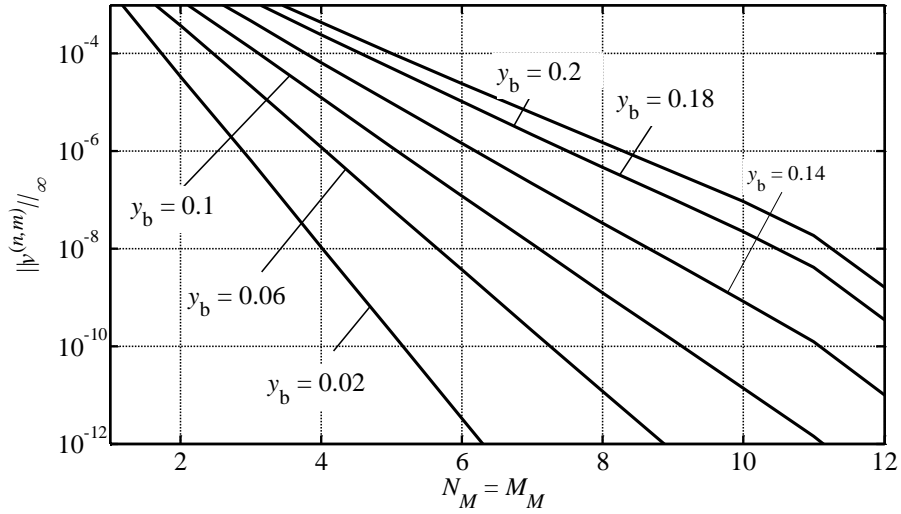


Figure 11: Variation of the Chebyshev norm of the modal function $v^{(n,m)}$ as a function of the Fourier mode index $n = m$ for the roughness geometry described by (6.1) with $\alpha = \beta = 1$ for $Re = 5$. Computations have been carried out with $N_M = M_M = 12$ Fourier modes and $N_T = 40$ Chebyshev polynomials.

An important aspect of the spectral accuracy involves the convergence of the truncated Fourier series describing the x - and z -variations of the flow field. Figure 10 shows that the algorithm delivers spectral accuracy in the x - and z -directions with increasing number of N_M and M_M respectively. Note that the magnitude of contributions of higher modes decreases exponentially. It is also noticeable that the maximum error of the solution

occurs at the boundary when sufficient number of Chebyshev polynomials is used. In other words

$$\|u_{er}\|_{\infty} = \|u_{er,BC}\|_{\infty}, \text{ when } \frac{\Delta}{\Delta N_T} (\|u_{er}\|_{\infty}) \approx 0. \quad (6.5)$$

The same relationship holds for other components of the velocity.

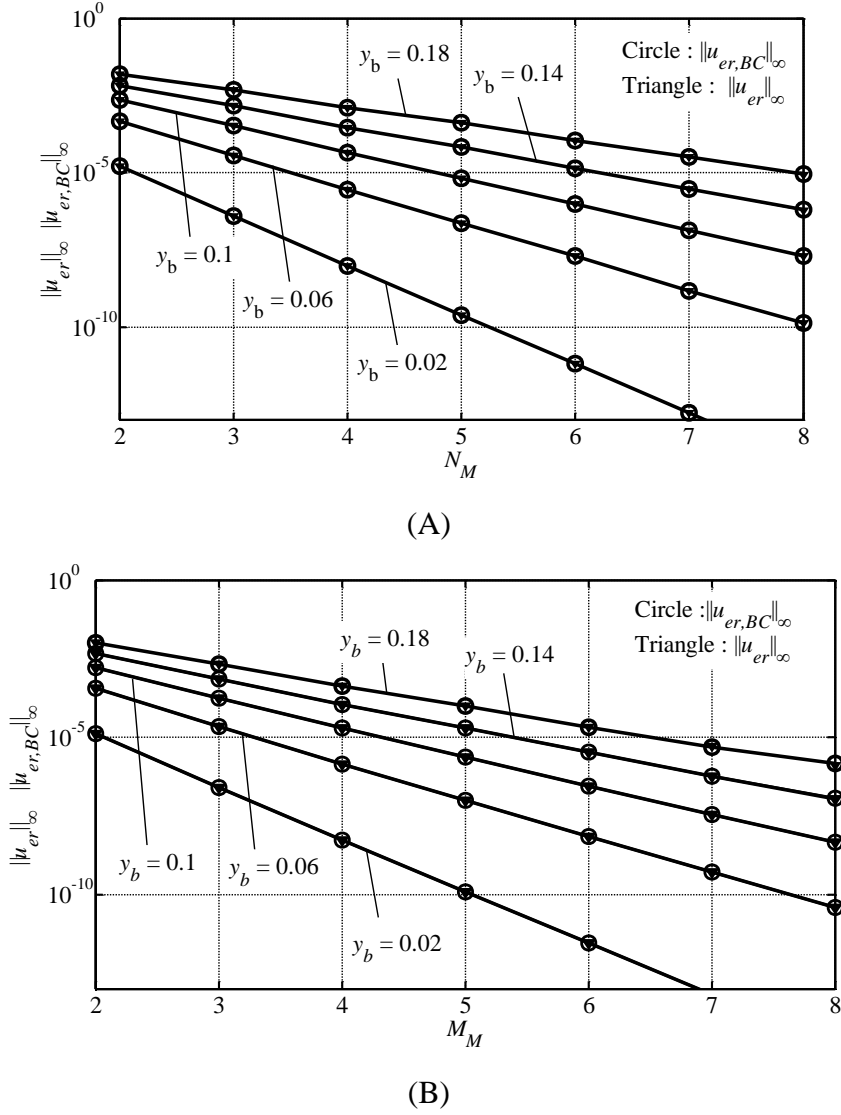
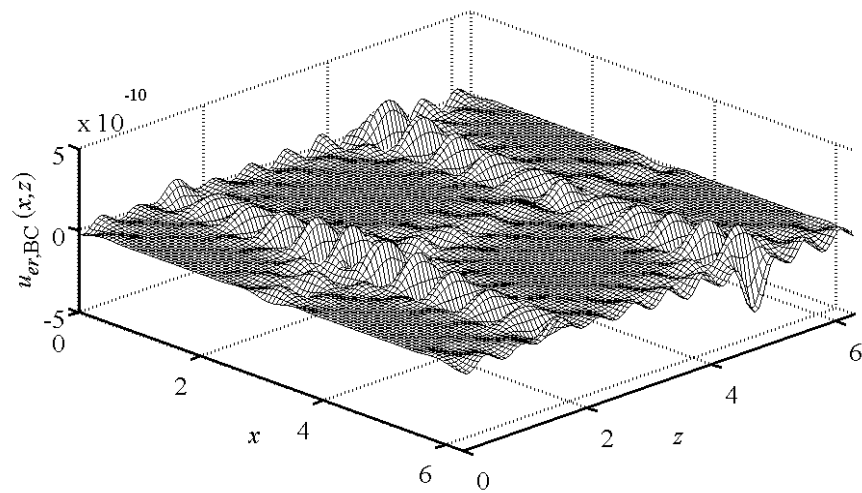
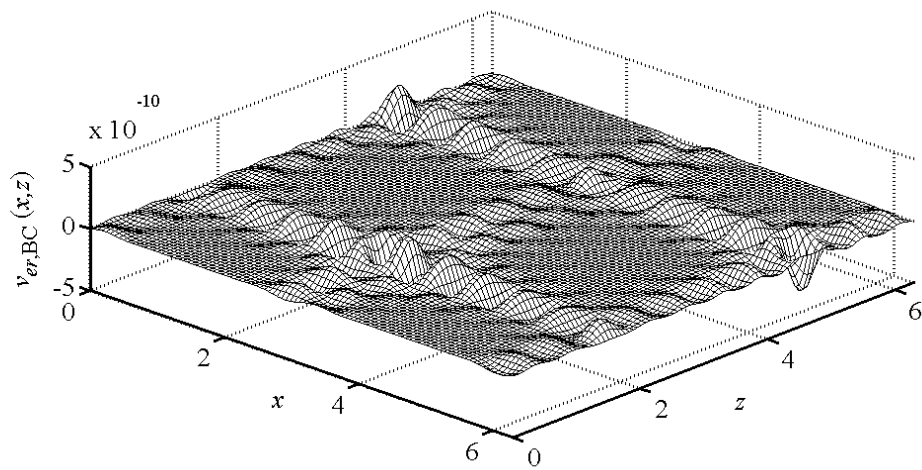


Figure 12: Variation of $\|u_{er}\|_{\infty}$ and $\|u_{er,BC}\|_{\infty}$ as a function of the number of Fourier modes used in the computations for the roughness geometry described by (5.1) with $\alpha = \beta = 1$ for $Re = 5$. Calculations have been carried out using $N_T = 40$, and $M_M = 10$ (Fig. 10A) and $N_M = 10$ (Fig. 10B).

Distributions of the boundary errors over a single period are illustrated in Fig. 11. The maxima are located at the largest channel opening. This fact can be explained by noting that all modal functions attain their maxima close to the maximum channel width. The contributions of the higher modes to the complete solution are largest at these locations and, thus, the rate of error reduction with an increase of the number of Fourier modes used in the solution is smaller. Increasing the wave number amplifies this effect due to the decrease of the thicknesses of the modal boundary layers.



(A)



(B)

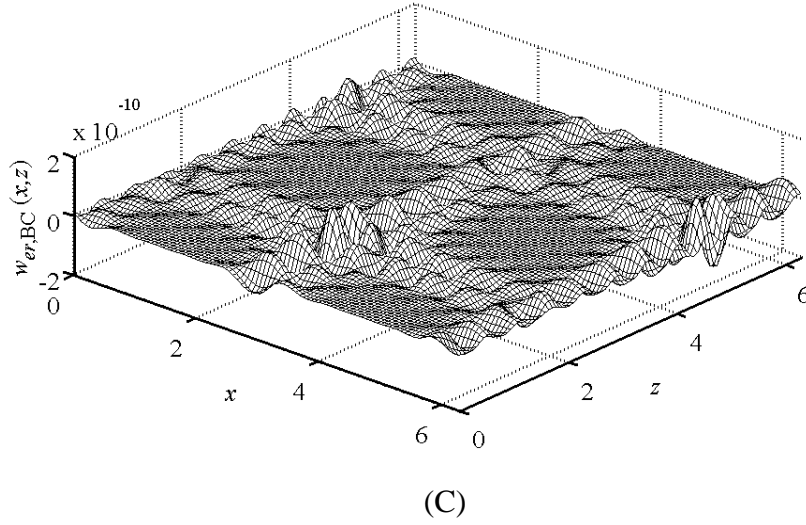


Figure 13: Distributions of the boundary errors $u_{er,BC}(x, z)$ (Fig. 11A), $v_{er,BC}(x, z)$ (Fig. 11B) and $w_{er,BC}(x, z)$ (Fig. 11 C) for the roughness geometry described by (5.1) with $\alpha = \beta = 1$ for $Re = 5$ over one period in the x - and z -directions.

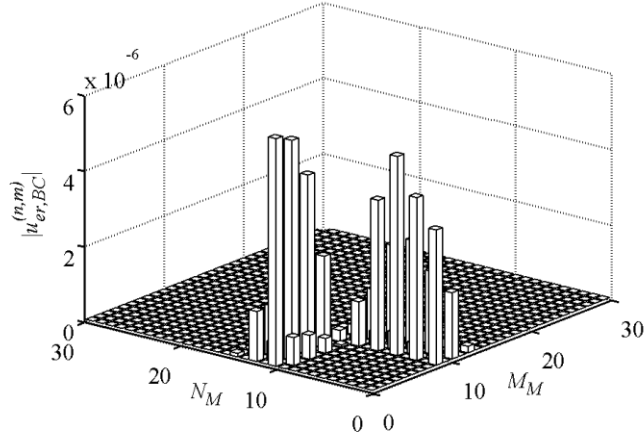
The construction of the boundary relation is based on the removal of all harmonics of the order lower than (N_M, M_M) . This property provides a test for the accuracy and consistency of the algorithm. The boundary error can be expressed by following Fourier expansions

$$u_{er,BC}(x, z) = \sum_{n=-\infty}^{\infty} \sum_{m=-\infty}^{\infty} u_{er,BC}^{(n,m)} e^{i(n\alpha x + m\beta z)}, \quad (6.6)$$

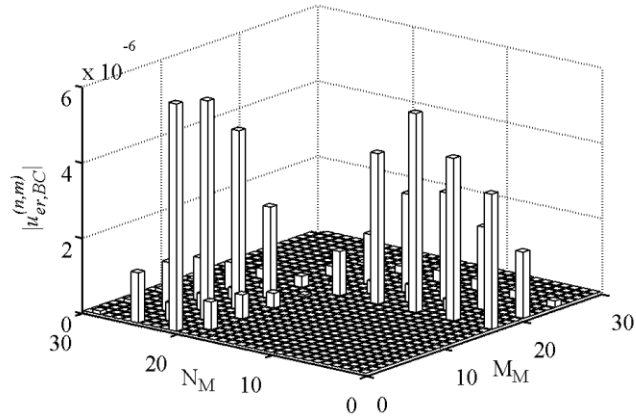
where $u_{er,BC}^{(n,m)}$ represent the Fourier expansion coefficients of the boundary error.

Spectral decomposition of the error at the rough wall displayed in Fig. 12A demonstrates the absence of the first 8 Fourier modes in the x -direction and first 7 Fourier modes in the z -direction which is in agreement with the theoretical basis underlying the construction of the boundary relations. Figure 12B displays the result of computation for the same conditions as in Fig. 12A but the computational box doubled in size in the periodic directions. The error spectrum has the same form as in Fig. 12A with the non-zero elements separated by zero elements as expected from the construction of the boundary

relations. These results demonstrate the absence of any spurious sub harmonics which could be potentially produced by the algorithm.



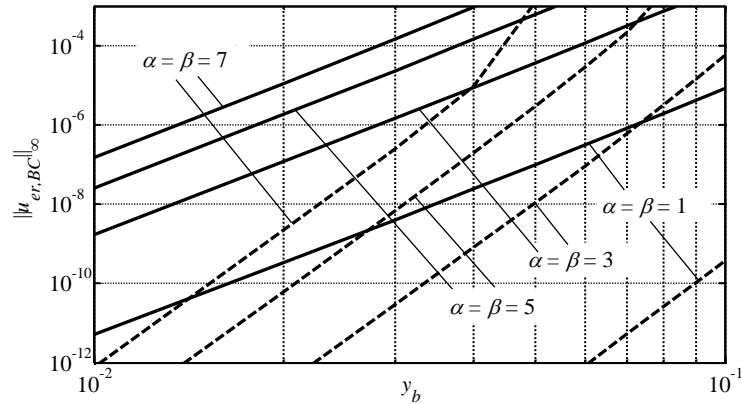
(A)



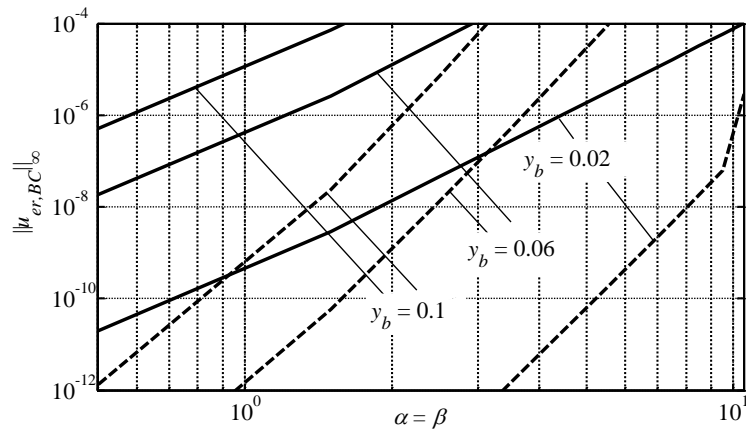
(B)

Figure 14: Spectral decomposition of $u_{er,BC}(x, z)$ for the roughness geometry described by (6.1) with $\alpha = \beta = 3$, $y_b = 0.1$ for $Re = 5$. Results displayed in Fig. 12A have been obtained using computational box with $\alpha = \beta = 3$, $N_M = 8$ and $M_M = 7$ Fourier modes and those displayed in Fig.12B have been obtained using computational box with $\alpha = \beta = 1.5$, $N_M = 16$ and $M_M = 14$ Fourier modes. In both cases, $N_T = 35$ Chebyshev polynomials were used.

The dependency of the boundary error on the wave numbers (or shape parameters) α and β and on the roughness amplitude y_b have been investigated. Results displayed in Fig.13 demonstrate that the error remains at the machine level for the wave numbers and amplitudes below a threshold value. The error increases exponentially when either the roughness amplitude or the roughness wave number surpasses this threshold. This threshold can be increased by increasing the number of Fourier modes used in the solution, however, the qualitative behavior of the error remains unchanged.



(A)



(B)

Figure 15: Variations of the error norm $\|u_{er,BC}\|_{\infty}$ as a function of the roughness amplitude y_b (Fig.13 A) and as a function of the roughness wave number with $\alpha = \beta$

(Fig.13 B) for the roughness geometry described by (6.1). Calculations have been carried out using $N_T = 40$ Chebyshev polynomials and $N_M = M_M = 5$ (solid lines) and $N_M = M_M = 10$ (dash lines) Fourier modes.

Effects of the Reynolds number can be assessed by studying variations of $\|u_{er,BC}\|_\infty$ displayed in Fig. 14. The error is unaffected by an increase of Re until Re reaches a certain threshold. The error starts to grow rapidly for Re above this threshold. The qualitative character of the error variations does not depend on the roughness amplitude but its magnitude increase with an increase of y_b .

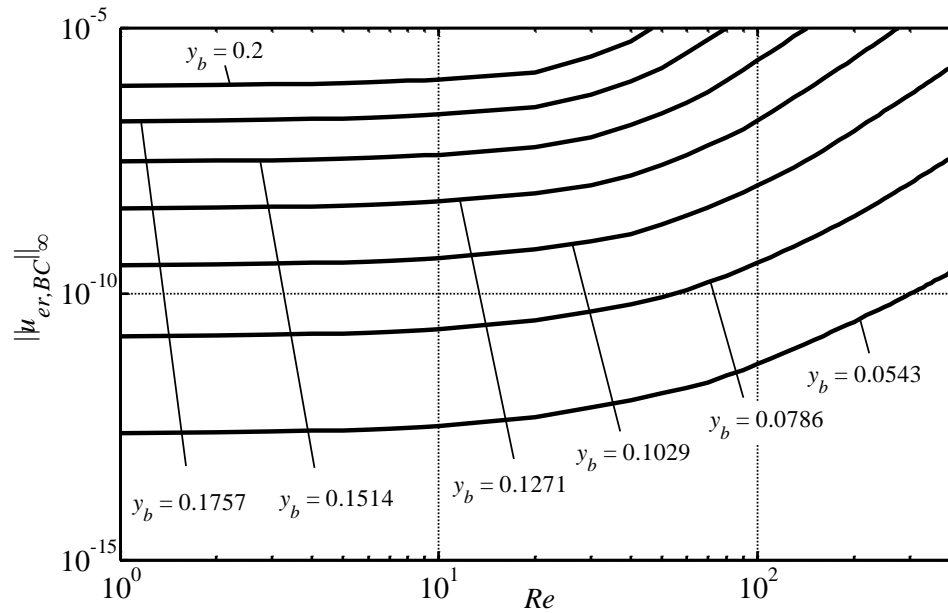


Figure 16: Variation of the error norm $\|u_{er,BC}\|_\infty$ as a function of the Reynolds number Re for the roughness geometry described by (6.1) with $\alpha = \beta = 1$ and different values of y_b . Computations have been carried out using $N_T = 50$ Chebyshev polynomials and $N_M = M_M = 10$ Fourier modes.

Section 7

7 Over-determined Formulation

Results displayed in Fig. 13 demonstrate that the error increases rapidly when a certain threshold expressed in terms of a combination of (α, β, y_b) is breached. The algorithm is based on two sets of Fourier expansions, one for the field variables and another one for the boundary conditions. The algorithm described above uses the same number of Fourier modes for the field equations and for the boundary conditions, and is sometimes referred to as the “classical formulation” [25]. When the roughness geometry becomes more extreme, the rate of convergence of expansion for boundary conditions slows down and this suggests the use of a larger number of terms from this expansion. Such an approach leads to an over-determined formulation as the number of equations (field equations and boundary relations) becomes larger than the number of unknowns. We shall now describe such a formulation.

The over-determined system is created using NM_o and MM_o Fourier modes in the x - and z -directions, respectively, in the construction of the boundary relations (3.30) where $-NM_o \leq n \leq NM_o$, $-MM_o \leq m \leq MM_o$ and $N_U \geq NM_o \geq N_M$ and $M_U \geq MM_o \geq M_M$. This results in $[(2NM_o + 1) \times (2MM_o + 1) \times (2N_T - 6) + 2]$ boundary relations. When $NM_o = N_M$ and $MM_o = M_M$ the system reduces to the classical form. The over-determined system can be written as

$$\mathbf{L}_0 \mathbf{X} = \mathbf{R}_0 \tag{7.1}$$

where \mathbf{L}_0 is the coefficient matrix of dimension $r \times p$ with $p = (2N_M + 1)(2M_M + 1)2N_T$ and $r = p + 6[(2NM_o + 1)(2MM_o + 1) - (2N_M + 1)(2M_M + 1)]$, \mathbf{X} is the vector of unknowns with dimension p and \mathbf{R}_0 is the r -dimensional right-hand side vector. Figure 15A illustrates the structure of \mathbf{L}_0 for $N_M = M_M = 1$, $NM_o = MM_o = 2$ and $N_T = 30$. For the efficient solution, the matrix is re-arranged by placing the entries corresponding to the field equations in matrix \mathbf{H} of size $q \times p$ with $q = [(2N_M +$

1)(2M_M + 1)(2N_T - 6) + 2] and entries corresponding to the boundary constraints in matrix \mathbf{K}_0 of size $(r - q) \times p$, following ideas described in [27]. \mathbf{H} has a block diagonal structure with each block having the size $(2N_T - 6) \times 2N_T$ whereas \mathbf{K}_0 is full and provides the coupling between the Fourier modes.

The system represented by (7.1) can only be solved in a least squares sense. The solution can be expressed as

$$\mathbf{X} = \mathbf{L}_0^+ \mathbf{R}_0 \quad (7.2)$$

where \mathbf{L}_0^+ represents the generalized inverse (or pseudo inverse) of \mathbf{L}_0 . Both QR factorization and Singular Value Decomposition (SVD) methods have been used to evaluate \mathbf{L}_0^+ . QR factorization is based on the decomposition of the matrix $\mathbf{L}_0 \in \mathbf{C}^{r \times p}$ into the product of a unitary matrix $\mathbf{Q} \in \mathbf{C}^{r \times r}$ and an upper triangular matrix $\mathbf{R} \in \mathbf{C}^{r \times p}$ in such a way that

$$\mathbf{L}_0 = \mathbf{QR} = \mathbf{Q} \begin{pmatrix} \mathbf{R}_1 \\ \mathbf{0} \end{pmatrix} \quad (7.3)$$

where $\mathbf{R}_1 \in \mathbf{C}^{p \times p}$ is an upper triangular matrix. The pseudo inverse \mathbf{L}_0^+ takes the following form

$$\mathbf{L}_0^+ = (\mathbf{R}_1^{-1} \quad \mathbf{0}) \mathbf{Q}^H \in \mathbf{C}^{p \times r} \quad (7.4)$$

where the superscript H stands for the conjugate transpose.

The singular value theorem states that for any matrix $\mathbf{L}_0 \in \mathbf{C}^{r \times p}$ of rank h , there exist unitary matrices $\mathbf{U} \in \mathbf{C}^{r \times r}$ and $\mathbf{V} \in \mathbf{C}^{p \times p}$ such that

$$\mathbf{L}_0 = \mathbf{USV}^H, \mathbf{S} = \begin{pmatrix} \mathbf{S}_1 & \mathbf{0} \\ \mathbf{0} & \mathbf{0} \end{pmatrix} \quad (7.5)$$

where $\mathbf{S} \in \mathbf{C}^{r \times p}$, $\mathbf{S}_1 = \text{diag}(\sigma_1, \sigma_2, \sigma_3, \dots, \sigma_h)$ and $\sigma_1 \geq \sigma_2 \geq \sigma_3 \geq \dots \geq \sigma_h > 0$.

In the above, σ_i represents the singular values of \mathbf{L}_0 . The pseudo inverse for this case has the form

$$\mathbf{L}_0^+ = \mathbf{V} \begin{pmatrix} \mathbf{S}_1^{-1} & \mathbf{0} \\ \mathbf{0} & \mathbf{0} \end{pmatrix} \mathbf{U}^H. \quad (7.6)$$

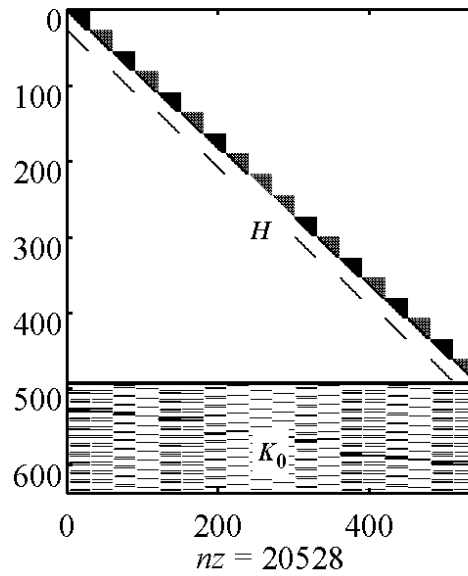
The efficient solver for the over-determined system is constructed in a similar manner as described in Section 4.1. The first step involves the extraction of the largest possible square matrix \mathbf{A} (Fig. 14B) of size $q \times q$ from \mathbf{H} . \mathbf{A} and \mathbf{B} are block diagonal whereas \mathbf{C}_0 and \mathbf{D}_0 are full and rectangular with dimensions $(r - q) \times q$ and $(r - q) \times (p - q)$, respectively. The system (7.1) can now be written as

$$\mathbf{A}\mathbf{X}_1 + \mathbf{B}\mathbf{X}_2 = (\mathbf{R}_0)_1, \quad \mathbf{C}_0\mathbf{X}_1 + \mathbf{D}_0\mathbf{X}_2 = (\mathbf{R}_0)_2 \quad (7.7)$$

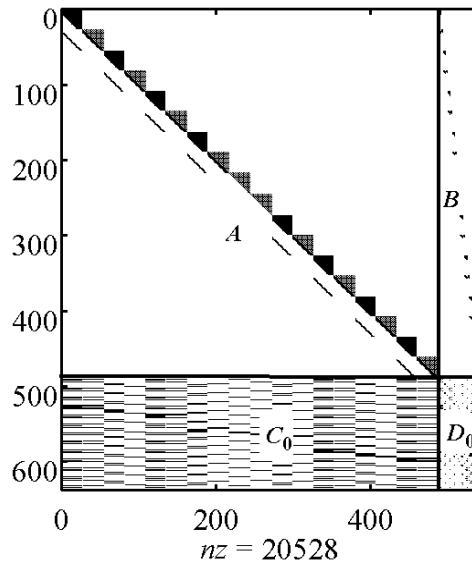
where \mathbf{X}_1 and \mathbf{X}_2 are the vector of unknowns and the right hand side vectors $(\mathbf{R}_0)_1$ and $(\mathbf{R}_0)_2$ have the sizes q and $(r - q)$ respectively. The solution of (7.8) can be written as

$$\mathbf{X}_2 = (\mathbf{D}_0 - \mathbf{C}_0\mathbf{A}^{-1}\mathbf{B})^+ [(\mathbf{R}_0)_2 - \mathbf{C}_0\mathbf{A}^{-1}(\mathbf{R}_0)_1], \quad \mathbf{X}_1 = \mathbf{A}^{-1}[(\mathbf{R}_0)_1 - \mathbf{B}\mathbf{X}_2]. \quad (7.8)$$

The block diagonal structure of \mathbf{A} and \mathbf{B} permits evaluation of $\mathbf{A}^{-1}(\mathbf{R}_0)_1$ and $\mathbf{A}^{-1}\mathbf{B}$ block by block leading to a significant reduction of the computational time and memory. Part of the system representing the field equations is solved exactly while the part representing the boundary conditions is solved in the least squares sense.



(A)



(B)

Figure 17: Structure of the coefficient matrix L_0 for the over-determined formulation with $N_M = M_M = 1$, $N_{M_o} = M_{M_o} = 2$ and $N_T = 30$. Black color represents the non-zero elements with nz denoting their number. Figure 15A displays the initial form of the matrix while Fig. 15B shows the form after extractions of the largest diagonal matrix A from H . The blocks assume various shades of grey depending on the density of the non-zero elements.

Figure 16 displays Fourier spectrum of the boundary error $u_{er,BC}(x, z)$ (see 6.3b). This error is distributed over several Fourier modes including modes with $(n, m) < (N_M, M_M)$ as expected from a least squares solution. Results displayed in Fig. 17 demonstrate that the over-determined formulation expands the applicability of the IBC method by about 30% measured in terms of both the roughness amplitude and the roughness wave number. This expansion can be partially attributed to the distribution of the boundary error over all modes associated with boundary relations, as illustrated in Fig.16. There is no noticeable difference between the solution obtained using the QR and SVD methods. There is an optimal number of boundary relations that provides the maximum gain and use of a larger number of such relations does not provide any benefits. This optimal number is approximately 50% bigger than the number of Fourier modes used for the discretization of the field equations.

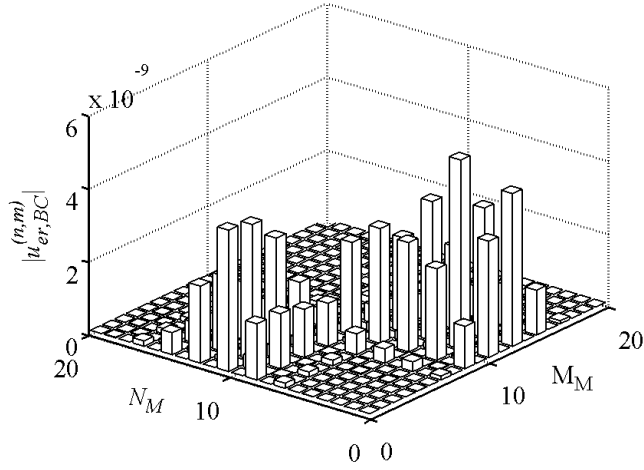
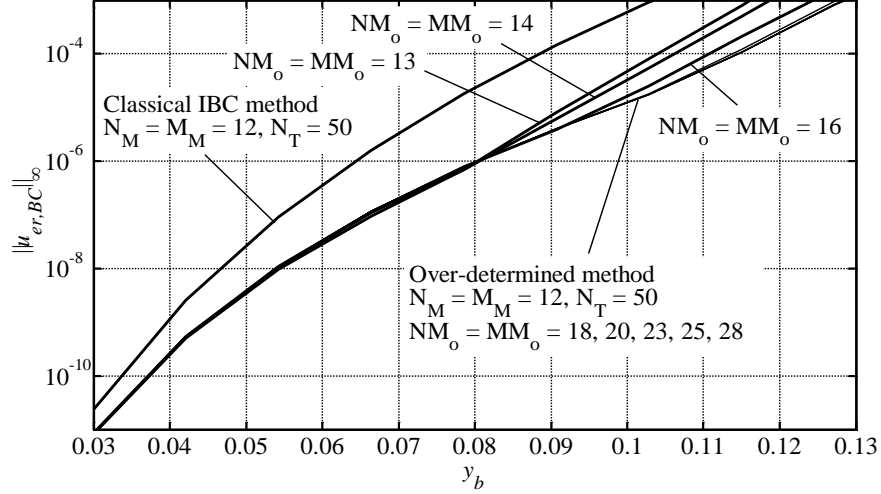
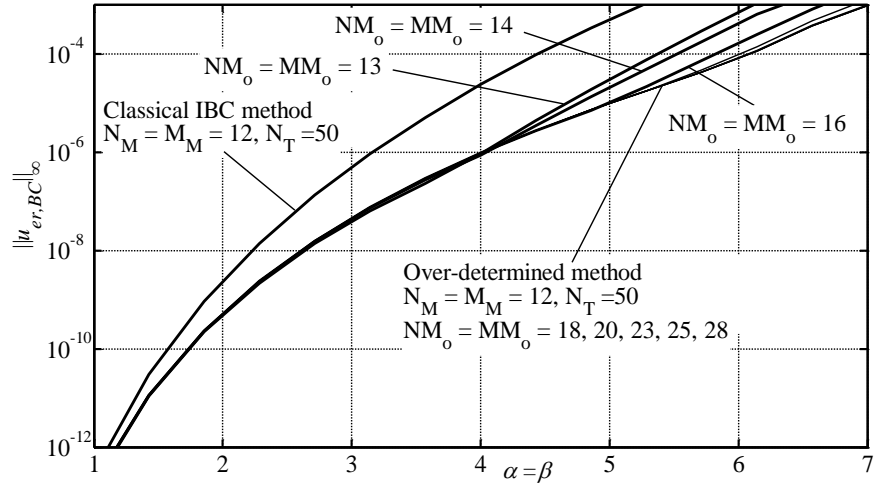


Figure 18: Spectral decomposition of $u_{er,BC}(x, z)$ at the rough wall for the roughness geometry described by (6.1) with $\alpha = \beta = 5$, $y_b = 0.05$ for $Re = 10$. Computations have been carried out using $N_T = 50$ Chebyshev polynomials, $N_M = M_M = 10$ Fourier modes for the field equations, and $MM_o = NM_o = 15$ Fourier modes for the boundary conditions.



(A)



(B)

Figure 19: Variations of the error norm $\|u_{er,BC}\|_{\infty}$ as a function of the roughness amplitude y_b (Fig.17 A) for the roughness geometry described by (6.1) with $\alpha = \beta = 4$ for $Re = 10$ and as a function of the roughness wave number $\alpha = \beta$ (Fig.17 B) for the roughness amplitude $y_b = 0.08$. Calculations have been carried out using $N_T = 50$ Chebyshev polynomials and $N_M = M_M = 12$ Fourier modes for the field equations.

Section 8

8 Limitations of the Algorithm

The IBC algorithm is highly accurate and delivers spectral accuracy but there are some limits to its applicability. The algorithm loses accuracy when the wall geometry becomes too extreme. Various tests reported in this thesis demonstrate that the extreme geometry, in the sense applicable to this algorithm, corresponds to large roughness amplitude and wave number. These problems can be overcome by using a larger number of Fourier modes combined with the over-determined formulation.

The algorithm uses Fourier expansions to represent wall geometry and, thus, all limitations associated with such expansions limit the performance of the algorithm. Geometries with corners and with segments characterized by infinite derivatives provide illustrative examples with difficulties more pronounced in the latter case due to the Gibb's phenomenon [44-46]. It has been found that use of a larger number of Fourier modes combined with the over-determined formulation and with the use of proper filtering techniques [47] can control the associated error.

The spectral accuracy of spatial discretization is independent of the Reynolds number. The increasing role of nonlinear effects at higher Reynolds numbers leads to an increase of the magnitude of the error but this can be counteracted through an increase in the number of Fourier mode and Chebyshev polynomials used in the computations. The convergence rate of the iterative process is linear as the first order fixed point iterative method is used and the rate of convergence slows down significantly for higher values of Re . Development of the second order iterative methods would address the problem of slow convergence in such situations.

Section 9

9 Conclusion

An efficient algorithm for the analysis of flows in rough channels has been developed. The algorithm is able to model any three-dimensional roughness shapes expressed in terms of Fourier expansions. The algorithm is based on the velocity-vorticity formulation and can accommodate the fixed flow rate constraints as well as the fixed pressure gradient constraints. The spatial discretization is based on the Fourier expansions in the streamwise and spanwise directions and on the Chebyshev expansions in the transverse direction. The domain irregularity associated with the roughness is accounted for by using the immersed boundary conditions (IBC) concept. The field equations are discretized using a computational domain in the form of a hexahedron while the rough channel is immersed inside this domain. The Galerkin procedure is used to develop algebraic equations corresponding to the field equations. The tau procedure is used for the inclusion of the flow boundary conditions. The forms of these conditions suitable for numerical computations have been constructed using Fourier expansions based on the shape of the rough wall resulting in the internal constraints which are then used to close the system of equations. The flow constraints are discretized with spectral accuracy and are solved simultaneously with the remaining equations. The discretization results in a gridless algorithm which permits efficient analysis of different patterns of surface roughness with minimal effort spend on geometry modelling. The nonlinear algebraic equations resulting from the discretization process are solved using the first-order fixed-point iterative method where the nonlinear terms are approximated using values from the previous iteration. A special linear solver has been developed based on taking advantage of the structure of the coefficient matrix. A method for reduction of the computational and memory requirements through the use of the complex conjugate property has been described. It has been demonstrated that the algorithm delivers spectral accuracy. The applicability of the algorithm is limited to roughness shapes that are not too extreme due to the reduction in the convergence rates of the Fourier expansions used for the

construction of the boundary relations. The algorithm applicability can be extended to more demanding geometries through inclusion of additional boundary relations leading to the over-determined formulation. In this case, the resulting system is solved in such a way that the part associated with the field equation is solved exactly while the part associated with the boundary relations is solved in the least squares sense. The best results are obtained when the number of boundary relations is approximately 50% greater than the number of Fourier modes used in the discretization of the field equation.

References

- [1] G. Hagen, *Über den einfluss der temperatur auf die bewegung des wassers in rohren*, Math. Abh. Akad. Wiss. (1854) 17-98.
- [2] H. Darcy, *Researches expérimentales relatives au mouvement de l'eau dans les tuyaux*, Mallet-Bachelier (1857).
- [3] J. Nikuradse, *Strömungsgesetze in Rauhen Rohren*, VDI-Forschungsheft 361 (1933); also NACA TM 1292 (1950).
- [4] L. F. Moody, *Friction factors for pipe flow*, Trans. ASME 66 (1944) 671–684.
- [5] M. J. Walsh, *Drag characteristics of V-groove and transverse curvature riblets*, In *Viscous Drag Reduction* (ed. G. R. Hough) AIAA 72 (1980) 168–184.
- [6] M. J. Walsh, *Riblets as a viscous drag reduction technique*, AIAA J. 21 (1983) 485–486.
- [7] H. Choi, P. Moin, & J. Kim, *On the effect of riblets in fully developed laminar channel flows*, Phys. Fluids A 3 (1991) 1892–1896.
- [8] D. C. Chu, & G. Karniadakis, *A direct numerical simulation of laminar and turbulent flow over riblet-mounted surfaces*, J. Fluid Mech. 250 (1993) 1–42.
- [9] I. Papautsky, J. Brazzle, T. Ameel, & A. B. Frazier, *Laminar fluid behavior in microchannels using micropolar fluid theory*, Sensors Actuators A 73 (1999) 101–108.
- [10] C. B. Sobhan, & S. V. Garimella, *A comparative analysis of studies on heat transfer and fluid flow in microchannels*, Microscale Therm. Engng. 5 (2001) 293–311.
- [11] G. L. Morini, *Single-phase convective heat transfer in microchannels: a review of experimental results*. Intl J. Therm. Sci. 43 (2004) 631–651.
- [12] K. V. Sharp, & R. J. Adrian, *Transition from laminar to turbulent flow in liquid filled microtubes*. Exp. Fluids 36 (2004) 741–747.

- [13] G. Gamrat, M. Favre-Marinet, S. Le Person, R. Baviere & F. Ayela, An experimental study and modelling of roughness effects on laminar flow in microchannels. *J. Fluid Mech.* 594 (2008) 399–423.
- [14] A. Mohammadi, J.M. Floryan, Pressure losses in grooved channels, *J. Fluid Mech.* 725 (2013) 23–54.
- [15] A. Mohammadi, J.M. Floryan, Groove optimization for drag reduction, *Phys. Fluids* 25 (2013) 113601.
- [16] S.Z. Husain, J.M. Floryan, Implicit spectrally-accurate method for moving boundary problems using immersed boundary conditions concept, *J. Comp. Phys.* 227 (2008) 4459–4477.

- [17] C.S. Peskin, The fluid dynamics of heart valves: experimental, theoretical and computational methods, *Annu. Rev. Fluid Mech.* 14 (1981) 235–259.
- [18] C.S. Peskin, The immersed boundary method, *Acta Numerica* 11 (2002) 479–517.
- [19] R. Mittal, G. Iaccarino, Immersed boundary methods, *Annu. Rev. Fluid Mech.* 37 (2005) 239–261.
- [20] J. Deng, X.M. Shao, A.L. Ren, A new modification of the immersed-boundary method for simulating flows with complex moving boundaries, *Int. J. of Num. Meth. Fluids* 52 (2006) 1195–1213.
- [21] K. Taira, T. Colonius, The immersed boundary method: a projection approach, *J. Comp. Phys.* 225 (2007) 2118–2137.
- [22] J. Kim, D. Kim, H. Choi, An immersed boundary finite-volume method for simulation of flows in complex geometries, *J. Comp. Phys.* 171 (2001) 132–150.
- [23] Y. Mori, Convergence proof of the velocity field for a Stokes flow immersed boundary method, *Commun. Pur. Appl. Math.* 61 (2008) 1213–1263.
- [24] A Liang, X. Jing, X. Sun, Constructing spectral schemes of the immersed interface method via a global description of discontinuous functions, *J. Comp. Phys.* 227 (2008) 8341–8366.
- [25] J. Szumbarski, J.M. Floryan, A direct spectral method for determination of flows over corrugated boundaries, *J. Comp. Phys.* 153 (1999) 378–402.

- [26] S.Z. Husain, J.M. Floryan, Immersed boundary conditions method for unsteady flow problems described by the Laplace operator, *Int. J. Num. Meth. Fluids* 56:9 (2007) 1765-1786.
- [27] S.Z. Husain, J.M. Floryan, Gridless spectral algorithm for Stokes flow with moving boundaries, *Comput. Methods Appl. Mech. Engrg.* 198 (2008) 245-259.
- [28] S.Z. Husain, J.M. Floryan, Spectrally-accurate algorithm for moving boundary problems for the Navier-Stokes equations, *J. Comp. Phys.* 229 (2010) 2287-2313.
- [29] S. Zandi, A. Mohammadi and J. M. Floryan, Spectrally-accurate algorithm for the analysis of flows in two-dimensional vibrating channels, *J. Comp. Phys.* 301 (2015) 425-455.
- [30] D.C.D.R. Fernandez, S.Z. Husain, J.M. Floryan, Immersed boundary conditions method for heat conduction in slots with time-dependent geometry. *Int. J. Num. Meth. Fluids* 67:4 (2011) 478-500.
- [31] H.V. Moradi, J.M. Floryan, Flows in annuli with longitudinal grooves, *J. Fluid Mech.* 716 (2013) 280–315.
- [32] J.M. Floryan, Centrifugal instability of Couette flow over a wavy wall, *Phys. Fluids* 14:1 (2002) 312-322.
- [33] J.M. Floryan, Vortex instability in a converging-diverging channel, *J. Fluid Mech.* 482 (2003) 17-50.
- [34] J.M. Floryan, C. Floryan, Traveling wave instability in a diverging-converging channel, *Fluid Dyn. Res.* 42 (2010) 025509.
- [35] J.M. Floryan, Three-dimensional instabilities of laminar flow in a rough channel and the concept of hydraulically smooth wall, *Eur. J. Mech. B/Fluids* 26 (2007) 305-329.
- [36] H.V. Moradi, J.M. Floryan, Stability of flow in a channel with longitudinal grooves, *J. Fluid Mech.* 757 (2014) 613–648.
- [37] A. Mohammadi, H. V. Moradi and J. M. Floryan, New instability mode in a grooved channel, *J. Fluid Mech.* 778 (2015) 691- 720.
- [38] J.M.Floryan, Flow in a Meandering Channel, *J. Fluid Mech.*, 770 (2015) 52-84.

- [39] S.Z. Husain, J.M. Floryan, J. Szumbariski, Over-determined formulation of the immersed boundary conditions method, *Comput. Methods Appl. Mech. Engrg.* 199 (2009) 94–112.
- [40] S.Z. Husain, J.M. Floryan, Effective solvers for the immersed boundaries method. *Computers & Fluids* 84 (2013) 127–140.
- [41] S.Z. Husain, J.M. Floryan, Efficient over-determined implementation of the immersed boundary conditions method, *Computers & Fluids* 105 (2014) 194–203.
- [42] P.R. Spalart, R.D. Moser, M.M. Rogers, Spectral methods for the Navier-Stokes equations with one infinite and two periodic directions, *J. Comp. Phys.* 96 (1991) 297-324.
- [43] A. Mohammadi, J. M. Floryan, Spectral Algorithm for Analysis of Flows in Grooved Channels, *Int. J. Num. Methods Fluids* 69 (2012) 606–638.
- [44] J. W. Gibbs, Fourier's Series, *Nature* 59 (1898) 200.
- [45] J. W. Gibbs, Fourier's Series, *Nature* 59 (1898) 606.
- [46] H. Wilbraham, On a certain periodic function, *The Cambridge and Dublin Mathematical Journal* 3 (1848) 198–201.
- [47] C. Canuto, M.Y. Hussaini, A. Quarteroni, T.A. Zang, *Spectral Methods: Fundamentals in Single Domains*, Springer-Verlag, Berlin Heidelberg, 2006.

Appendices

Appendix A

Analysis of Mode (0,0)

Modal equations for mode (0,0) for the wall-normal vorticity and velocity can be obtained using the modal form of the definition of the wall-normal vorticity and the continuity equation. These have the form of

$$im\beta u^{(n,m)} - in\alpha w^{(n,m)} = \eta^{(n,m)}, \quad (\text{A.1})$$

$$in\alpha u^{(n,m)} + Dv^{(n,m)} + im\beta w^{(n,m)} = 0 \quad (\text{A.2})$$

and reduce for $(n, m) = (0,0)$ to

$$\eta^{(0,0)} = 0, \quad (\text{A.3})$$

$$Dv^{(0,0)} = 0. \quad (\text{A.4})$$

The second equation gives

$$v^{(0,0)} = \text{constant} = c_1. \quad (\text{A.5})$$

The total flow rate for one period through any plane parallel to the x - z plane is proportional to $v^{(0,0)}$ and, therefore, is constant. This can be demonstrated as follows

$$\begin{aligned} Q_y &= \int_0^{2\pi/\beta} \int_0^{2\pi/\alpha} v_1(x, y, z) dx dz \\ &= \int_0^{2\pi/\beta} \int_0^{2\pi/\alpha} \sum_{n=-\infty}^{\infty} \sum_{m=-\infty}^{\infty} v^{(n,m)}(y) e^{i(n\alpha x + m\beta z)} dx dz \\ &= \frac{2\pi}{\beta} \int_0^{2\pi/\alpha} \left[\sum_{n=-\infty}^{\infty} v^{(n,0)}(y) e^{in\alpha x} dx \right] + \\ &\quad \int_0^{2\pi/\beta} \left[\sum_{n=-\infty}^{\infty} \sum_{\substack{m=-\infty \\ m \neq 0}}^{\infty} \frac{1}{im\beta} v^{(n,m)}(y) e^{in\alpha x} (e^{i2\pi m} - 1) \right] dx \end{aligned}$$

$$\begin{aligned}
&= \frac{4\pi^2}{\alpha\beta} v^{(0,0)}(y) + \frac{2\pi}{\beta} \sum_{\substack{n=-\infty \\ n \neq 0}}^{\infty} \frac{1}{in\alpha} v^{(n,0)}(y) (e^{i2\pi n} - 1) \\
&= \frac{4\pi^2}{\alpha\beta} v^{(0,0)} = \text{constant} = c_2.
\end{aligned} \tag{A.6}$$

Since the net flow rate in the transverse direction is zero, it can be concluded that

$$v^{(0,0)} = 0. \tag{A.7}$$

Appendix B

Determination of Chebyshev Expansion Coefficient for a Known Modal Function

A known modal function $G^{(n,m)}$ can be expressed in terms of the Chebyshev expansion of the form

$$G^{(n,m)}(\hat{y}) = \sum_{k=0}^{N_T-1} G_k^{(n,m)} T_k(\hat{y}) \tag{B.1}$$

where $G_k^{(n,m)}$ are the expansion coefficients. In order to compute $G_k^{(n,m)}$, we evaluate $G^{(n,m)}(\hat{y})$ at N_T Chebyshev points along \hat{y}_l . This results in a system of N_T equations of the form

$$[T_k(\hat{y}_l)] \{G_k^{(n,m)}\} = \{G^{(n,m)}(\hat{y}_l)\} \tag{B.2}$$

whose solution determines $G_k^{(n,m)}$.

Appendix C

Evaluation of Fourier expansions representing periodic functions formed by the values of the Chebyshev polynomials, its derivatives and the reference flow velocity evaluated along the rough boundary

Functions formed by values of the Chebyshev polynomials and its derivative evaluated along the upper wall are expressed as Fourier expansions of the form given by (3.40a)-(3.40b). Use of the recurrence relation (3.28) and the Fourier representation of the wall geometry (3.9a) results in the relations of the form

$$(CU)_{k+1}^{(n,m)} = 2 \sum_{p=-N_A}^{N_A} \sum_{q=-M_A}^{M_A} A_U^{(n,m)} (CU)_k^{(n-p,m-q)} - (CU)_{k-1}^{(n,m)}, \quad k \geq 1, \quad (C.1)$$

$$(CU)_0^{(0,0)} = 1, (CU)_0^{(n,m)} = 0, |(n,m)| \geq 1, (CU)_1^{(n,m)} = A_U^{(n,m)} \quad \text{for } |(n,m)| \geq 0 \quad (C.2)$$

which permit evaluation of all required Fourier coefficients in (3.40a). A similar process applied to the derivative of the Chebyshev polynomials and use of (3.30) result in the following relations

$$(EU)_{k+1}^{(n,m)} = 2 \sum_{p=-N_A}^{N_A} \sum_{q=-M_A}^{M_A} A_U^{(n,m)} (EU)_k^{(n-p,m-q)} - (EU)_{k-1}^{(n,m)} + 2(CU)_k^{(n,m)} \quad \text{for } k \geq 2, \quad (C.3)$$

$$(EU)_0^{(n,m)} = 0 \quad \text{for } |(n,m)| \geq 0, \quad (C.4)$$

$$(EU)_1^{(0,0)} = 1, (EU)_1^{(n,m)} = 0 \quad \text{for } |(n,m)| \geq 1 \quad \text{and} \quad (EU)_2^{(n,m)} = 4A_U^{(n,m)} \quad \text{for } |(n,m)| \geq 0 \quad (C.5)$$

which permit evaluation of all required Fourier coefficients in (3.40b). In order to evaluate the Fourier expansion coefficients of the function formed by the values of the u -component of the reference velocity evaluated along the rough wall, one starts with (3.32) of the form

$$u_0(\hat{y}_U(x, z)) = \frac{2}{Re} e_x(-a\hat{y}_U^2 - 2ab\hat{y}_U + 1 - b^2), \quad (C.6)$$

expresses \hat{y}_U using (3.9a), evaluates \hat{y}_U^2 with the help of (3.9a) resulting in the following relation

$$\hat{y}_U^2 = \sum_{n=-N_A}^{N_A} \sum_{m=-M_A}^{M_A} \sum_{p=-N_A}^{N_A} \sum_{q=-M_A}^{M_A} A_U^{(n,m)} A_U^{(n-p,m-q)} e^{i(n\alpha x + m\beta z)}, \quad (\text{C.7})$$

substitutes (3.9a) and (C.7) into (C.6), separates Fourier components and compares the resulting expression with (3.40c) resulting in the following relations for the Fourier coefficients required in (3.40c)

$$(U_0^U)^{(n,m)} = \frac{2}{Re} e_x \left[-a^2 \sum_{p=-N_A}^{N_A} \sum_{q=-M_A}^{M_A} A_U^{(p,q)} A_U^{(n-p,m-q)} - 2abA_U^{(n,m)} \right],$$

$$\text{for } 1 \leq |(n,m)| \leq 2N_{A,U} \quad (\text{C.8})$$

$$(U_0^U)^{(0,0)} = \frac{2}{Re} e_x \left[-a^2 \sum_{p=-N_A}^{N_A} \sum_{q=-M_A}^{M_A} A_U^{(p,q)} A_U^{(p,q)*} - 2abA_U^{(n,m)} + (1 - b^2) \right]$$

$$\text{for } (n,m) = (0,0). \quad (\text{C.9})$$

A similar process applied to the w -component of the reference velocity results in the following expressions for the Fourier coefficients required in (3.40d)

$$(W_0^U)^{(n,m)} = \frac{2}{Re} e_z \left[-a^2 \sum_{p=-N_A}^{N_A} \sum_{q=-M_A}^{M_A} A_U^{(p,q)} A_U^{(n-p,m-q)} - 2abA_U^{(n,m)} \right],$$

$$\text{for } 1 \leq |(n,m)| \leq 2N_A \quad (\text{C.10})$$

$$(W_0^U)^{(0,0)} = \frac{2}{Re} e_z \left[-a^2 \sum_{p=-N_A}^{N_A} \sum_{q=-M_A}^{M_A} A_U^{(p,q)} A_U^{(p,q)*} - 2abA_U^{(n,m)} + (1 - b^2) \right]$$

$$\text{for } (n,m) = (0,0). \quad (\text{C.11})$$

Curriculum Vitae

Name: Md Nazmus Sakib

Post-secondary Education and Degrees: Bangladesh University of Engineering and Technology
Dhaka, Bangladesh
2007-2012 BSc (Mechanical Engineering).

The University of Western Ontario
London, Ontario, Canada
2014-2016 M.E. Sc. (Mechanical and Materials Engineering)

Honours and Awards: Western Graduate Research Scholarship
2014-2016

Related Work Experience Teaching and Research Assistant
The University of Western Ontario
2014-2016

Publications (Journal):

N. Sakib, A. Mohammadi and J. M. Floryan, “Spectrally Accurate Immersed Boundary Conditions Method for Three-Dimensional Flows”, submitted for publication in the Journal of Computational Physics. Manuscript Number: JCOMP-D-15-01411.

Publications (Conferences):

Sakib, Md., Floryan, J. M. (2015) “Three-Dimensional Spectrally-Accurate Algorithm for the Navier-Stokes Equations”. *Proceedings of the 25th Canadian Congress of Applied Mechanics (CANCAM2015)*, May 31–June4, London, Ontario, Canada.

Sakib, Md., Floryan, J. M. (2015) “Analysis of Flow over 3D Surface Topography”. *Thousand Islands Fluid Dynamics Meeting (TIM 2015)*, May1–3, Gananoque, Ontario, Canada.